A Microstructural Electrochemo-mechanical Model of High-nickel Composite Electrodes Towards Digital Twins to Bridge the Particle and Electrode-Level Characterizations

Jihun Song[a], Royal C Ihuaenyi[a], Jaejin Lim[b], Zihan Wang[c], Wei, Li[a], Ruqing Fang[a], Amin Kazem Ghamsari[a], Hongyi Xu[c], Yong Min Lee[b,**], Juner Zhu[a,*]

[a]*Department of Mechanical and Industrial Engineering, Northeastern University, Boston, MA 02115, United States of America*

[b]*Department of Chemical and Biomolecular Engineering, Yonsei University, Seoul 03722, Republic of Korea*

[c]*Department of Mechanical Engineering, University of Connecticut, Storrs, CT 06269, United States of America*

Keywords: Microstructure, Plastic deformation, Lithium-induced strain and stress, operando electrochemo-mechanical analysis, Conductive and binder domain, Mechanical degradation

***Corresponding author**

Email: j.zhu@northeastern.edu

**** Corresponding author**

Email: yongmin@yonsei.ac.kr

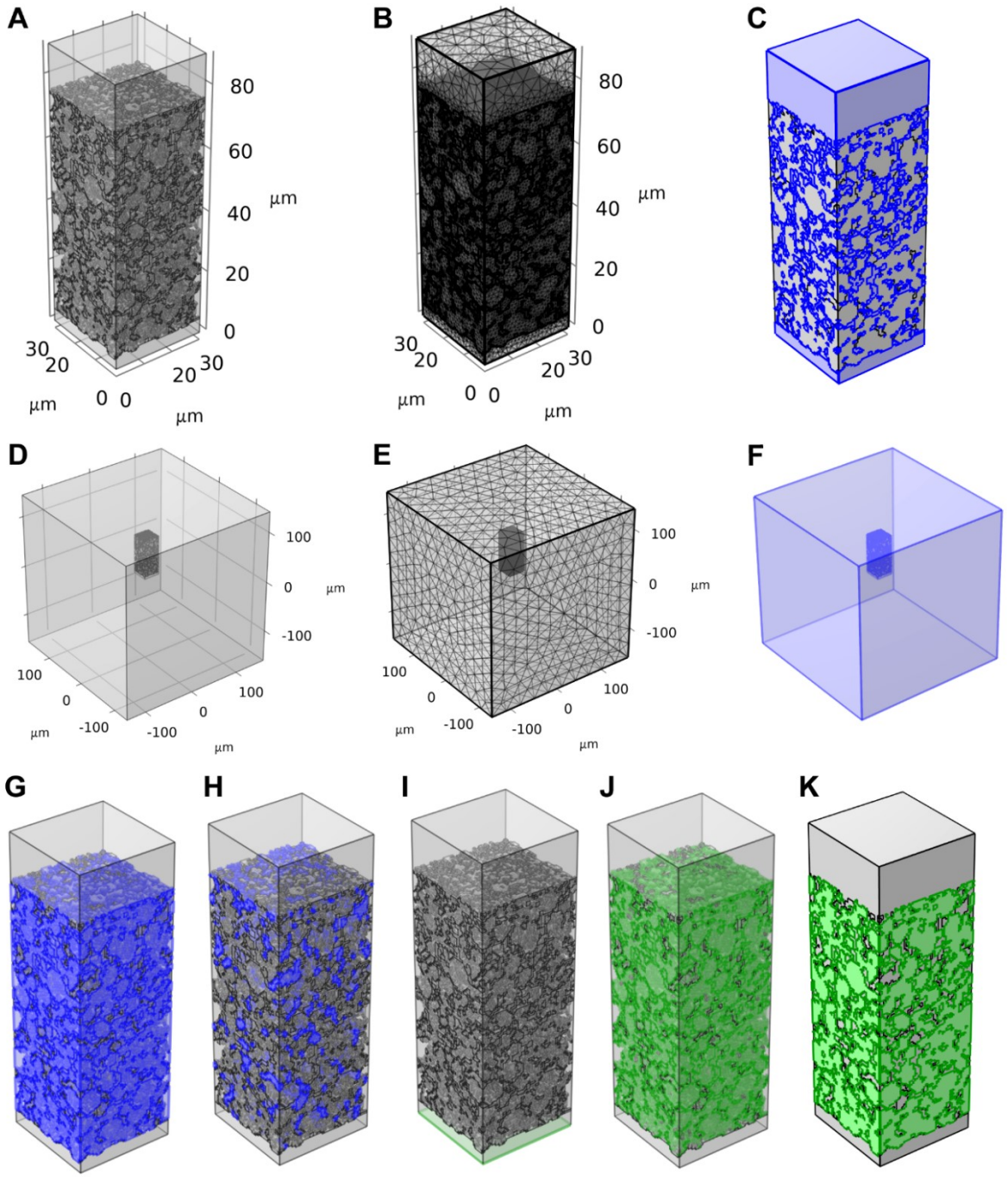

Fig. S1. Geometries, mech, boundaries and domains under the realistic electrode condition and excessive electrolyte condition.

(A) Geometries under the realistic electrode condition.
(B) Meshes under the realistic electrode condition.
(C) Electrolyte domains under the realistic electrode condition.
(D) Geometries under the excessive electrolyte.
(E) Meshes under the excessive electrolyte.
(F) Electrolyte domains under the excessive electrolyte.
(G) Domains of active materials.
(H) Domains of Conductive and binder materials.
(I) Boundaries of current flow and fixed surface.
(J) Boundaries of reaction site for the electrochemical modeling.
(K) Symmetric boundaries for the electrochemical modeling.

Rate capability comparison in coin cells and microelectrode model.

We utilized active material parameters fitted using a particle model without fitting any parameters for the cathode. However, due to the high energy density and fast charge rate of this cathode, the overpotential at the lithium metal anode significantly influences cell performance. To quantify the overpotentials during the plating process, we fabricated a pouch-type lithium metal three-electrode cell and applied currents of 1C (2.38 mA cm^{-2}), 2C (4.77 mA cm^{-2}), and 4C (9.54 mA cm^{-2}) for 15 minutes, resulting in average overpotentials of 0.1092 V, 0.2261 V, and 0.3124 V, respectively (Fig. S2). By applying these overpotentials to the anode, the model achieved an accuracy of more than 98% across all C-rates (Fig. S3).

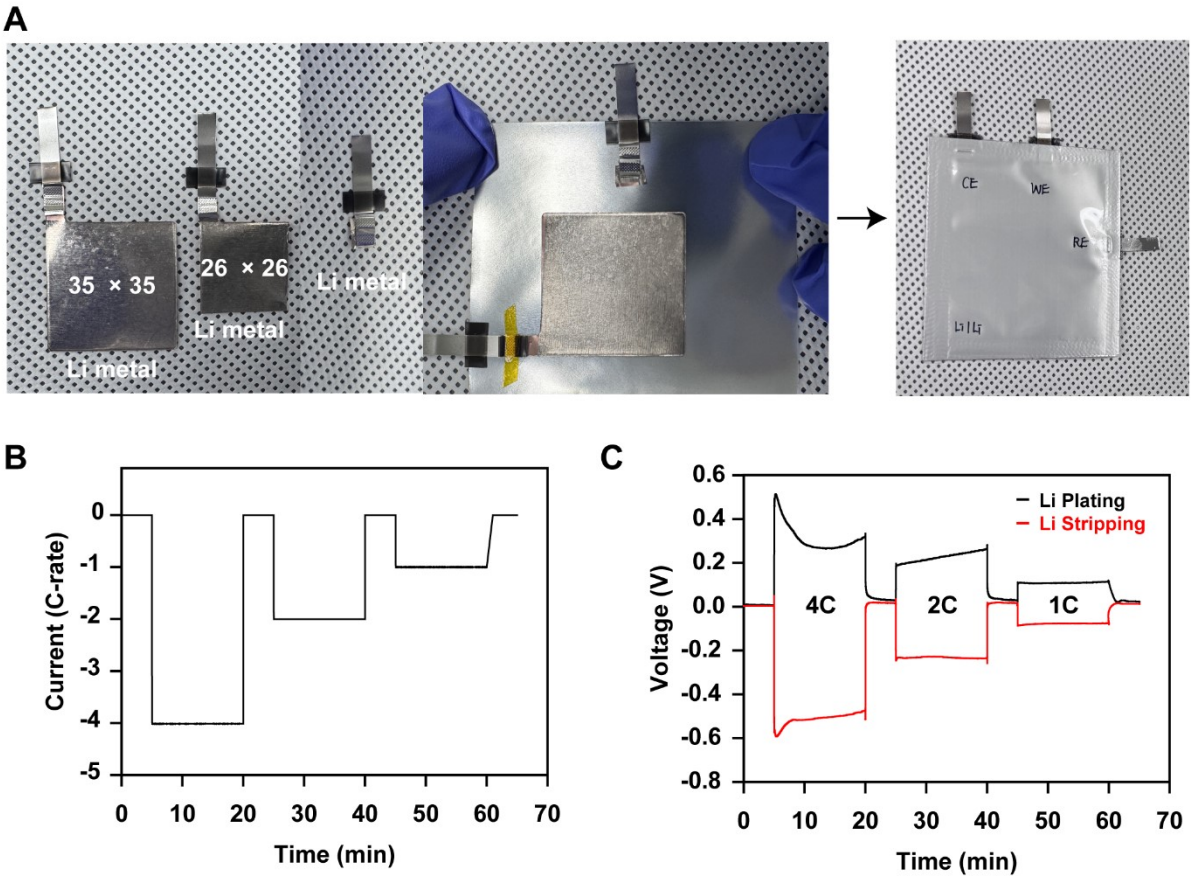

Fig. S2. Lithium metal three-electrode test
(A) Fabrication process of the three-electrode cell
(B) Applied currents for the overpotential measurement over 15 minutes: 1C (2.38 mA cm^{-2}), 2C (4.77 mA cm^{-2}), and 4C (9.54 mA cm^{-2}).
(C) Overpotentials observed during lithium plating and lithium stripping over 15 minutes.

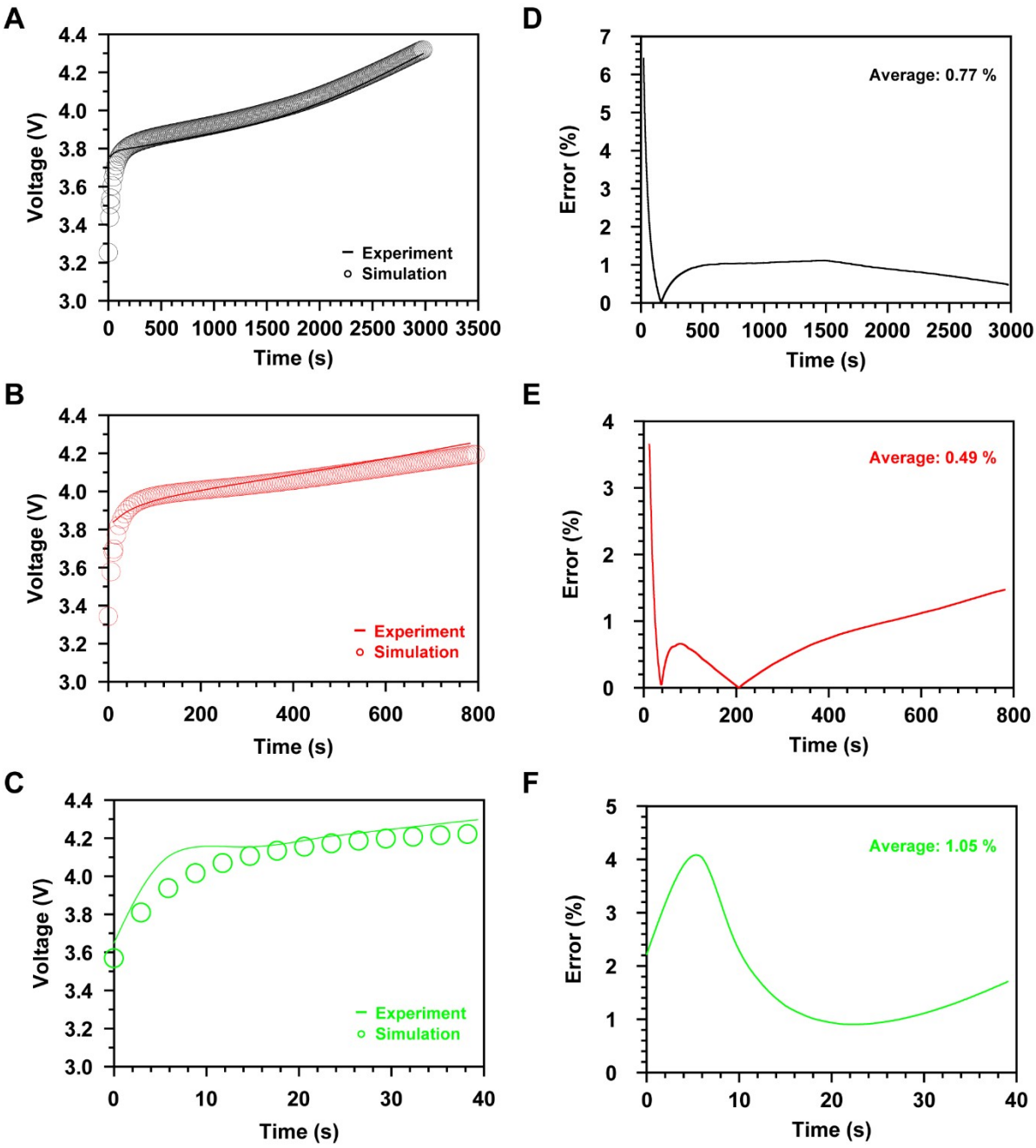

Fig. S3. Model verification by comparing charge voltage profiles of coin cells and the simulation model.

(A) Charge voltage profiles measured in the coin cell and simulated by the model at 1C.
(B) Charge voltage profiles measured in the coin cell and simulated by the model at 2C.
(C) Charge voltage profiles measured in the coin cell and simulated by the model at 4C.
(D) Voltage error of the experimental data and the simulation data at 1C.
(E) Voltage error of the experimental data and the simulation data at 2C.
(F) Voltage error of the experimental data and the simulation data at 4C.

3D operando structural, electrochemical, and mechanical analysis

During the charging process, the 3D operand analysis was performed when the 25%, 50%, 75%, and cutoff voltages were reached at 1C, 2C, and 4C under the realistic electrode condition and the excessive electrolyte condition (Fig. S4-S30).
A larger gradient of lithium-ion concentration occurred under the realistic electrode conditions compared to excessive electrode conditions (Fig. S4-S12). The gradient of lithium-ion concentration causes the large overpotential (Fig. S13-S15) and the strain gradient. Additionally, this strain can change the current flow throughout the electrode (Fig. S16-S18) and finally causes high stress in (Fig. S19-S30)

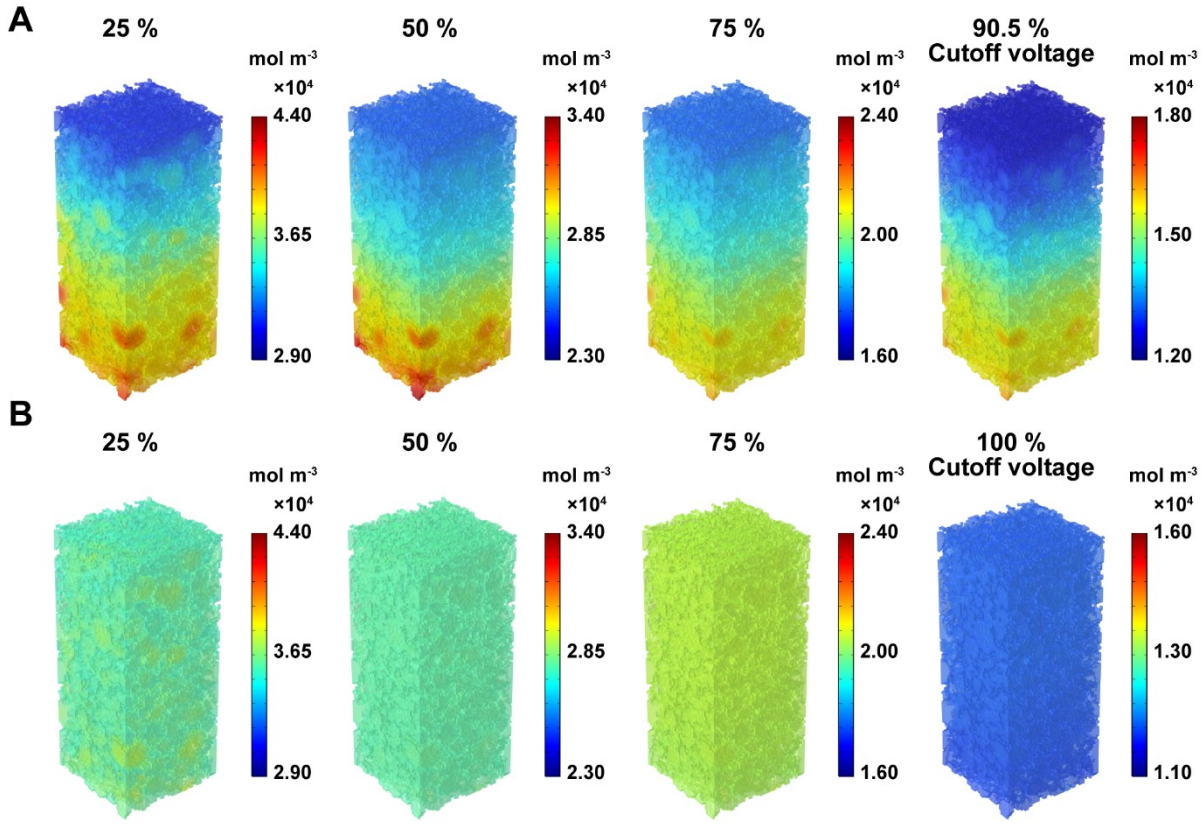

Fig. S4. 3D operando analysis of lithium-ion concentrations in active materials during charging at 1C under the realistic electrode condition and excessive electrolyte condition.
(A) 3D operando analysis of lithium-ion concentration in active materials charged by 1C under the realistic electrode condition.
(B) 3D operando analysis of lithium-ion concentration in active materials charged by 1C under the excessive electrolyte condition.

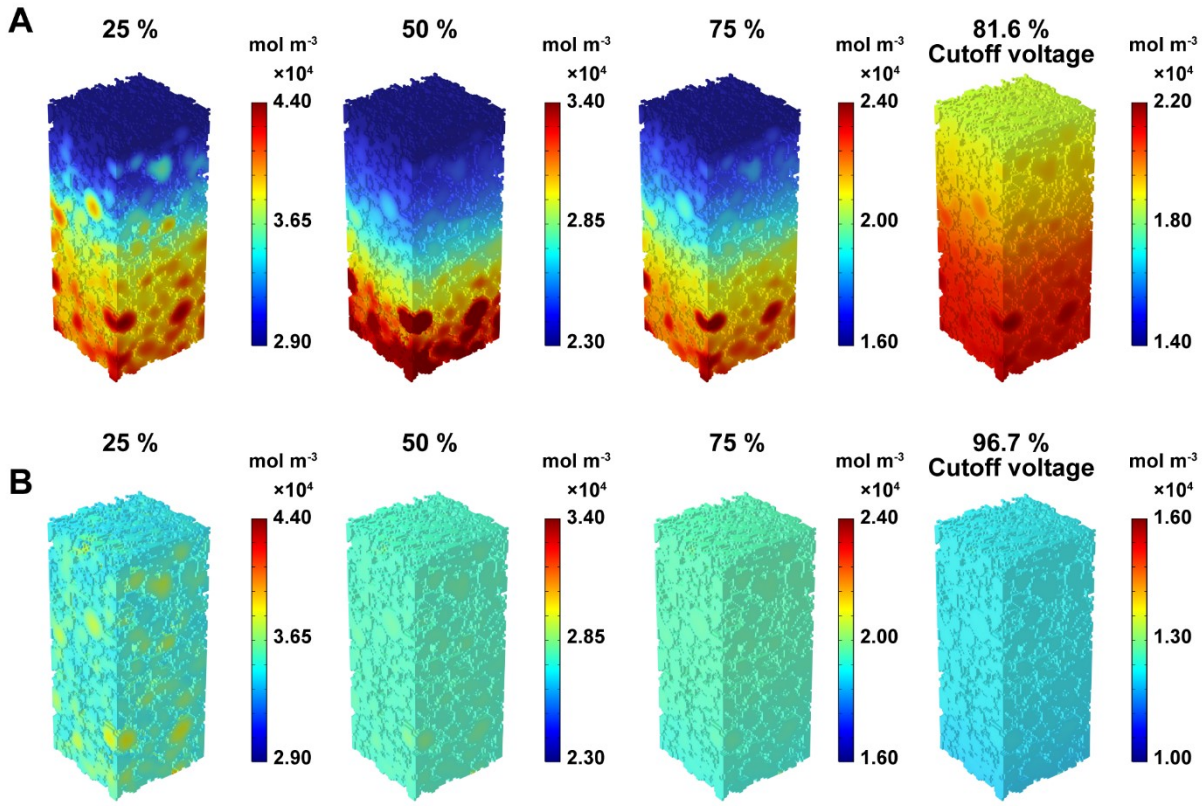

Fig. S5. 3D operando analysis of lithium-ion concentrations in active materials during charging at 2C under the realistic electrode condition and excessive electrolyte condition.
(A) 3D operando analysis of lithium-ion concentration in active materials charged by 2C under the realistic electrode condition.
(B) 3D operando analysis of lithium-ion concentration in active materials charged by 2C under the excessive electrolyte condition.

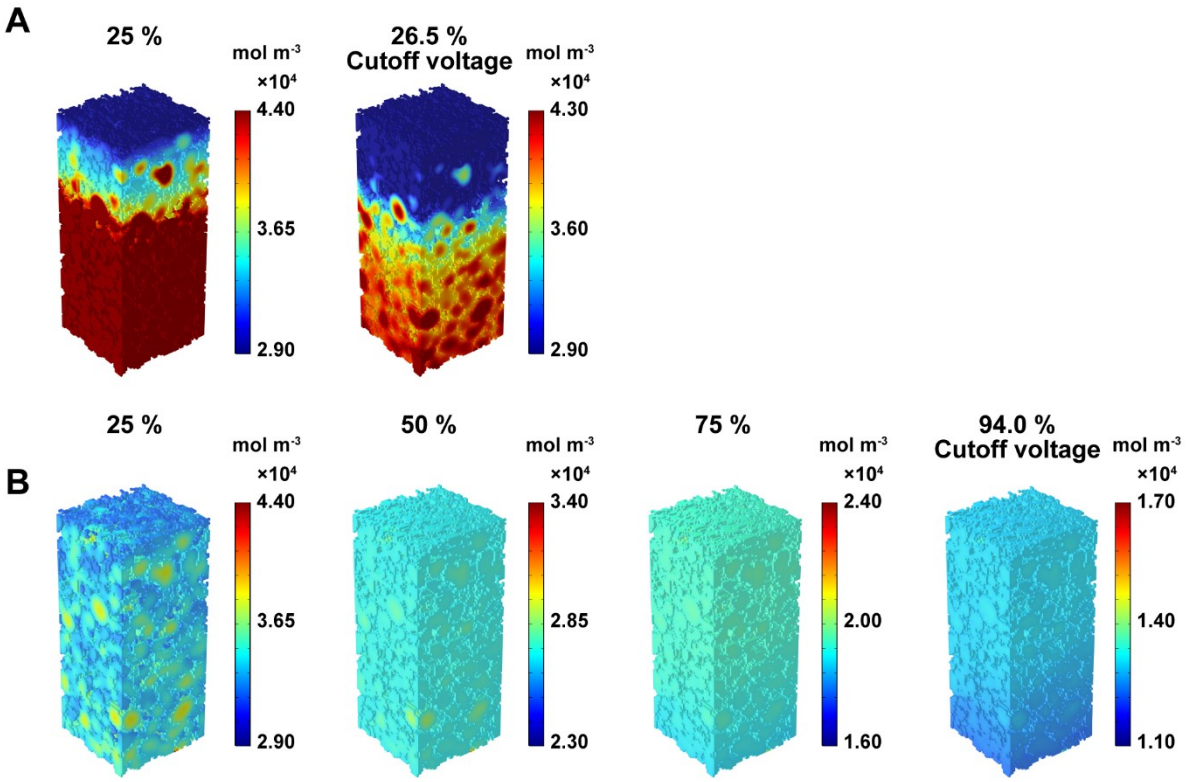

Fig. S6. 3D operando analysis of lithium-ion concentrations in active materials during charging at 4C under the realistic electrode condition and excessive electrolyte condition.
(A) 3D operando analysis of lithium-ion concentration in active materials charged by 4C under the realistic electrode condition.
(B) 3D operando analysis of lithium-ion concentration in active materials charged by 4C under the excessive electrolyte condition.

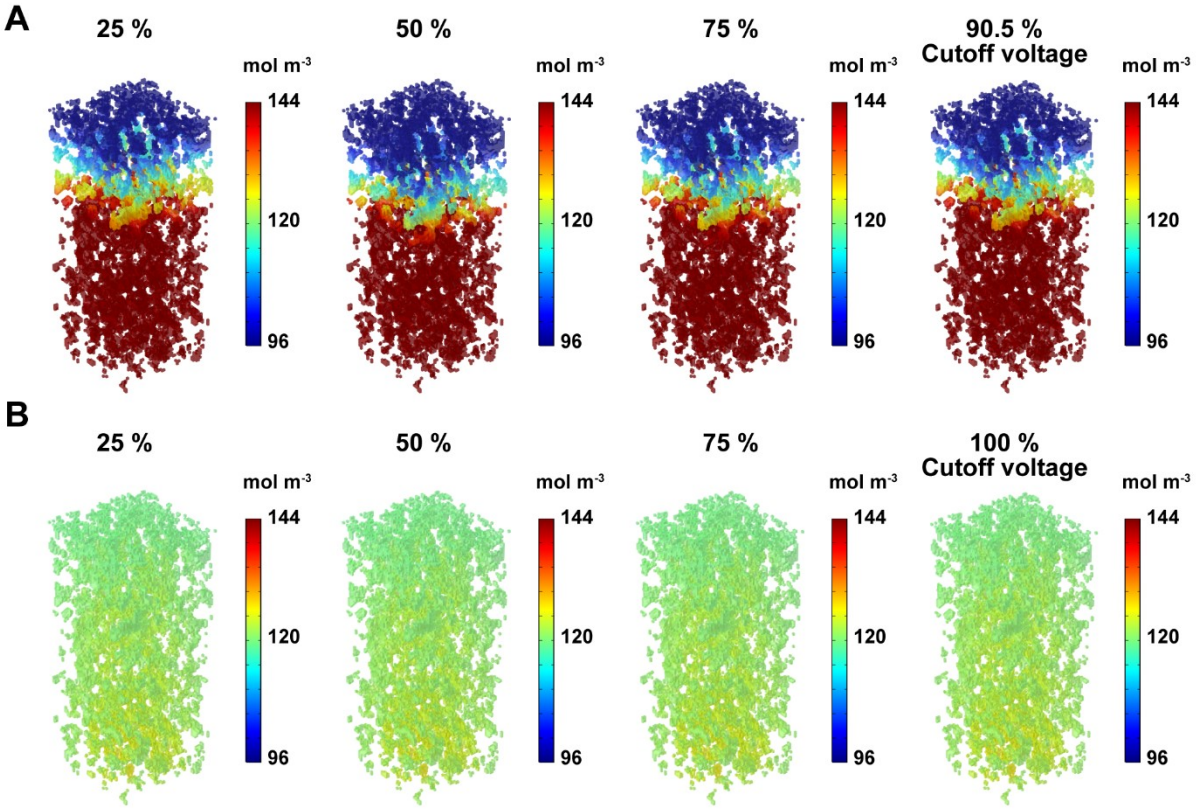

Fig. S7. 3D operando analysis of lithium-ion concentrations in conductive and binder materials during charging at 1C under the realistic electrode condition and excessive electrolyte condition.

(A) 3D operando analysis of lithium-ion concentration in conductive and binder materials charged by 1C under the realistic electrode condition.

(B) 3D operando analysis of lithium-ion concentration in conductive and binder materials charged by 1C under the excessive electrolyte condition.

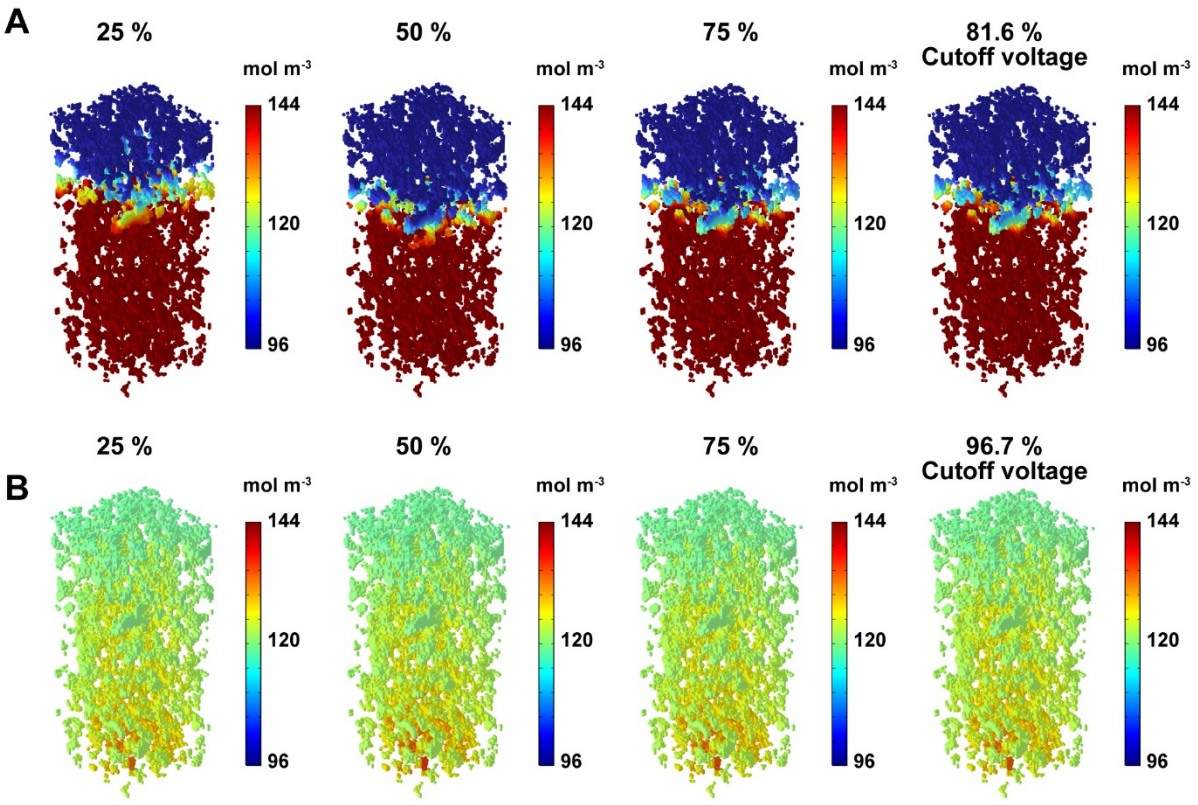

Fig. S8. 3D operando analysis of lithium-ion concentrations in conductive and binder materials during charging at 2C under the realistic electrode condition and excessive electrolyte condition.

(A) 3D operando analysis of lithium-ion concentration in conductive and binder materials charged by 2C under the realistic electrode condition.

(B) 3D operando analysis of lithium-ion concentration in conductive and binder materials charged by 2C under the excessive electrolyte condition.

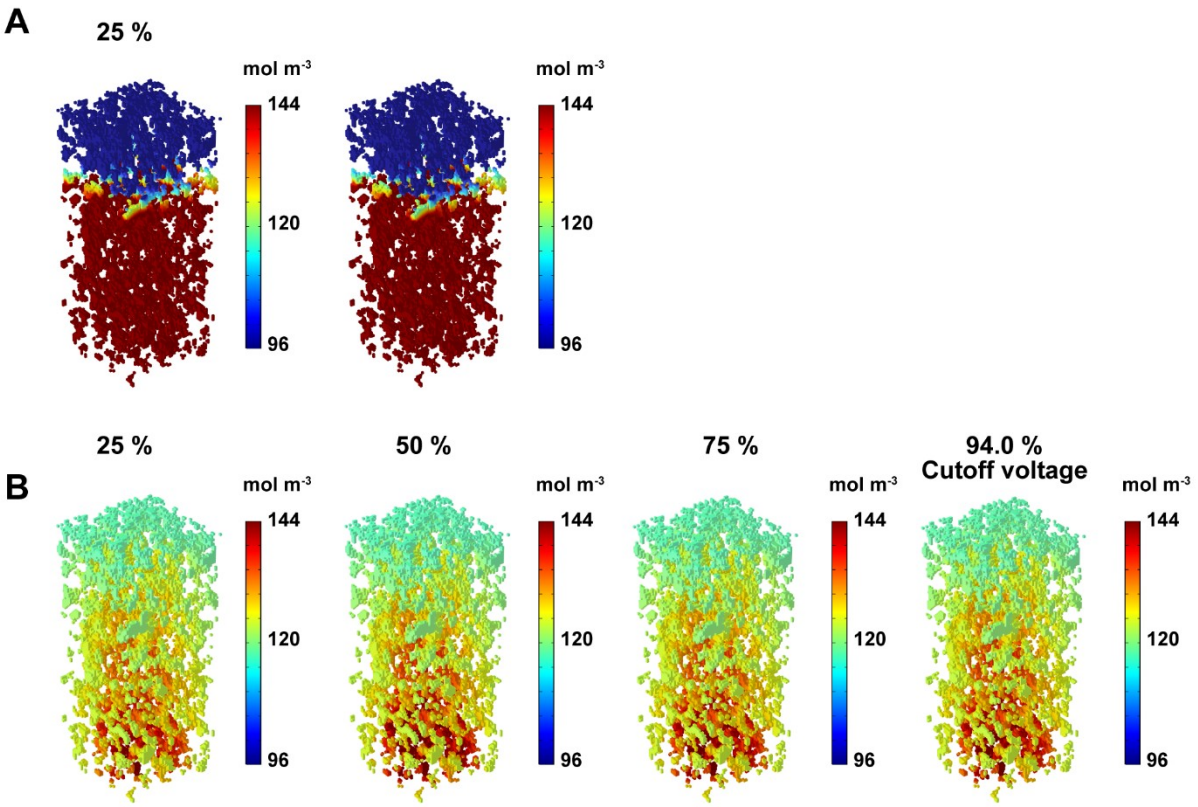

Fig. S9. 3D operando analysis of lithium-ion concentrations in conductive and binder materials during charging at 4C under the realistic electrode condition and excessive electrolyte condition.

(A) 3D operando analysis of lithium-ion concentration in conductive and binder materials charged by 4C under the realistic electrode condition.

(B) 3D operando analysis of lithium-ion concentration in conductive and binder materials charged by 4C under the excessive electrolyte condition.

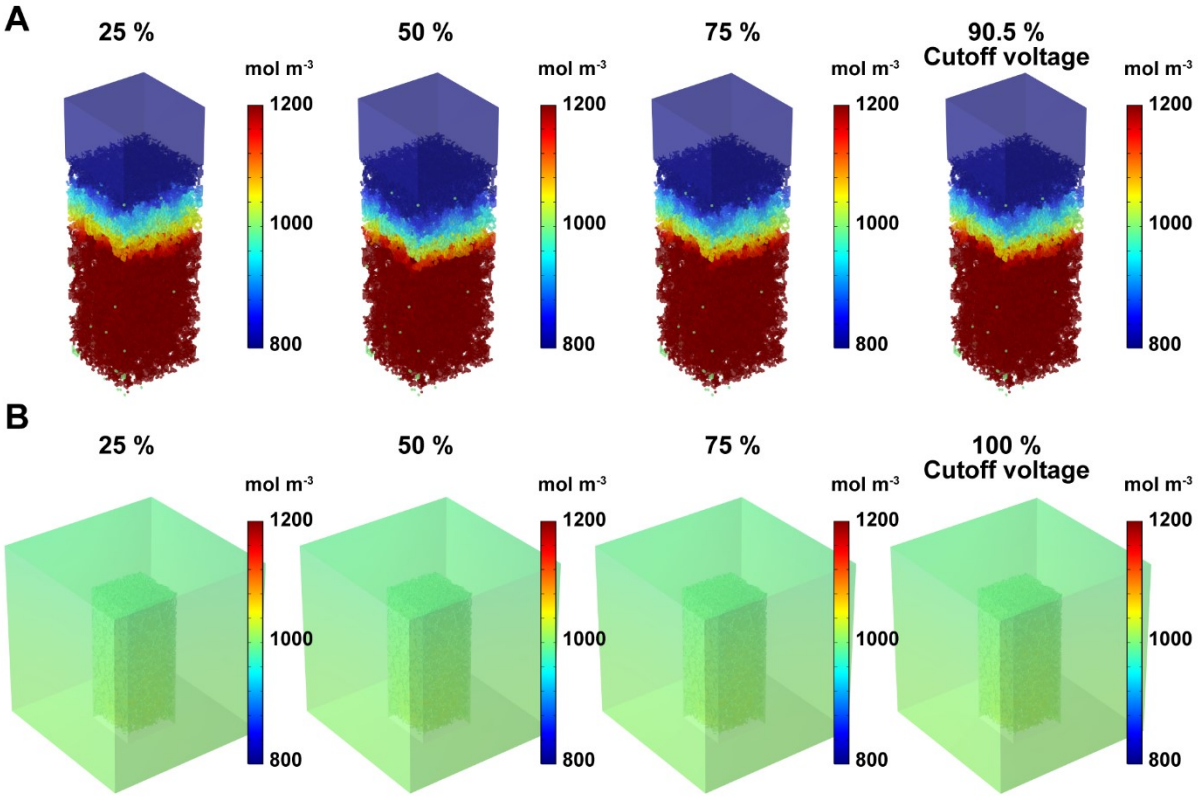

Fig. S10. 3D operando analysis of lithium-ion concentrations in the electrolyte during charging at 1C under the realistic electrode condition and excessive electrolyte condition.
(A) 3D operando analysis of lithium-ion concentration in the electrolyte charged by 1C under the realistic electrode condition.
(B) 3D operando analysis of lithium-ion concentration in the electrolyte charged by 1C under the excessive electrolyte condition.

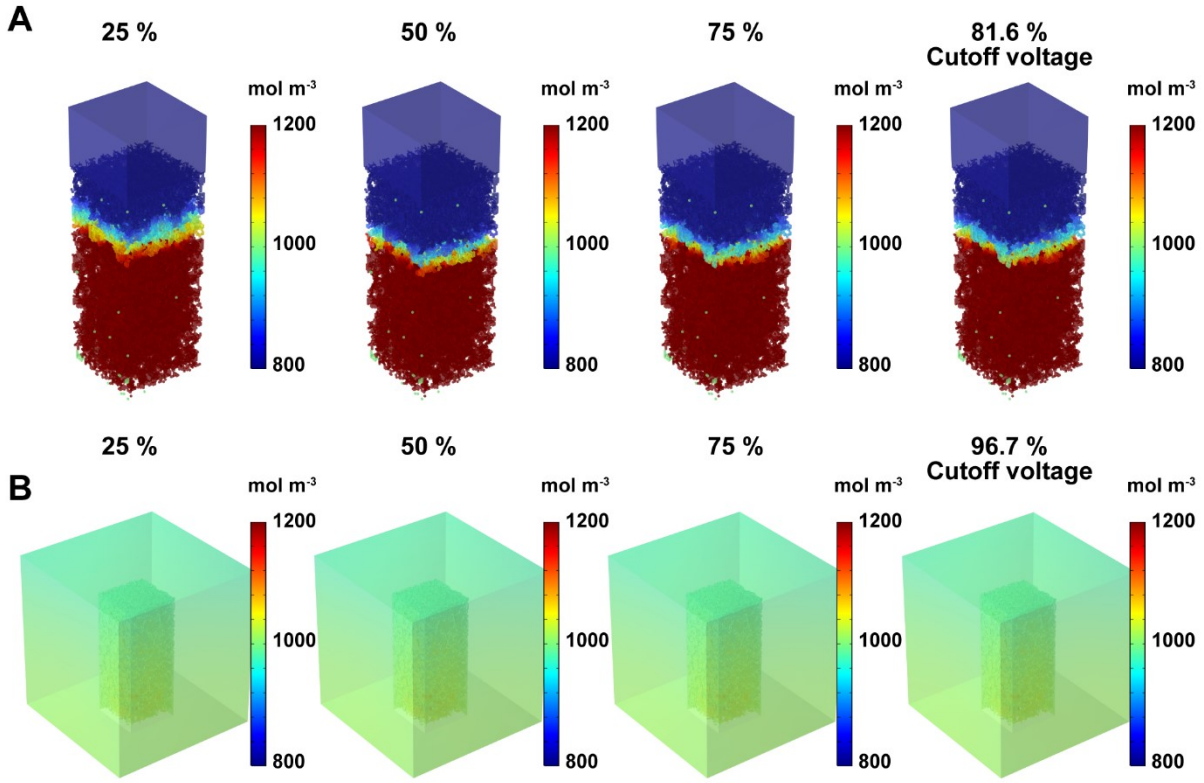

Fig. S11. 3D operando analysis of lithium-ion concentrations in the electrolyte during charging at 2C under the realistic electrode condition and excessive electrolyte condition.
(A) 3D operando analysis of lithium-ion concentration in the electrolyte charged by 2C under the realistic electrode condition.
(B) 3D operando analysis of lithium-ion concentration in the electrolyte charged by 2C under the excessive electrolyte condition.

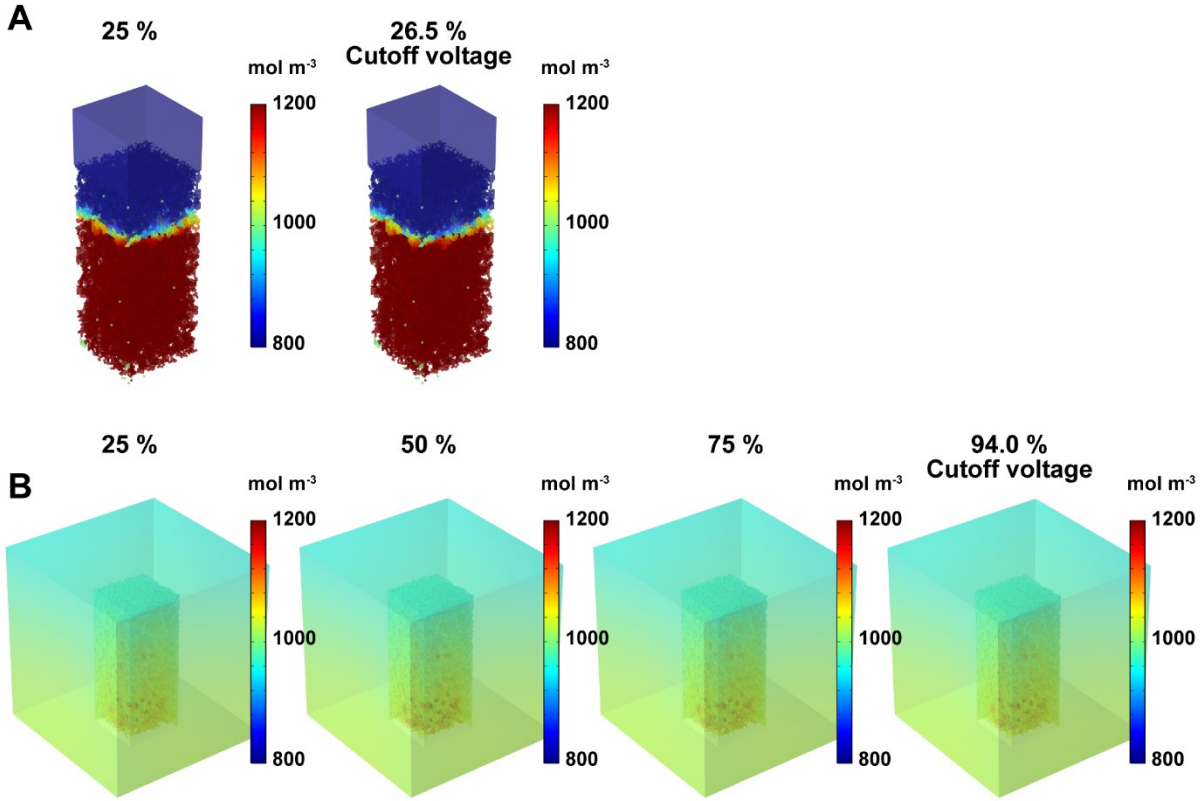

Fig. S12. 3D operando analysis of lithium-ion concentrations in the electrolyte during charging at 4C under the realistic electrode condition and excessive electrolyte condition.
(A) 3D operando analysis of lithium-ion concentration in the electrolyte charged by 4C under the realistic electrode condition.
(B) 3D operando analysis of lithium-ion concentration in the electrolyte charged by 4C under the excessive electrolyte condition.

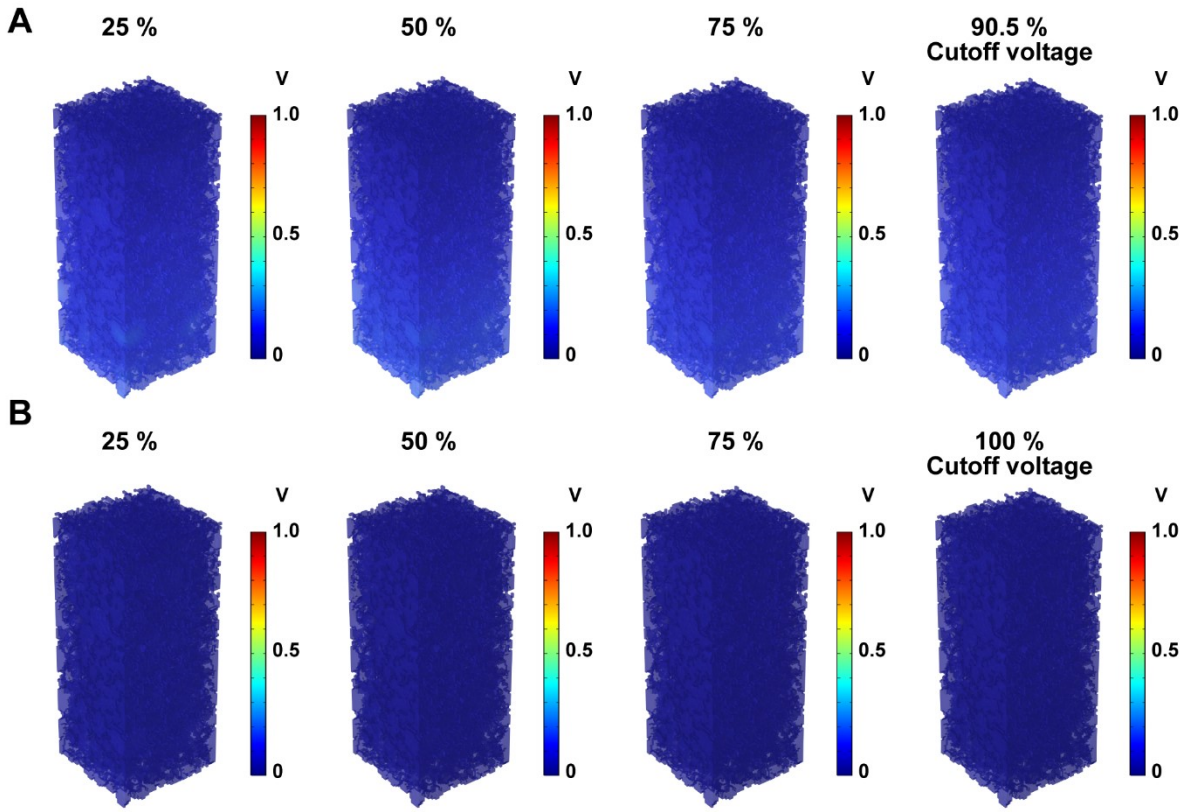

Fig. S13. 3D operando analysis of overpotentials in the active materials during charging at 1C under the realistic electrode condition and excessive electrolyte condition.
(A) 3D operando analysis of overpotential in active materials charged by 1C under the realistic electrode condition.
(B) 3D operando analysis of overpotential in active materials charged by 1C under the excessive electrolyte condition.

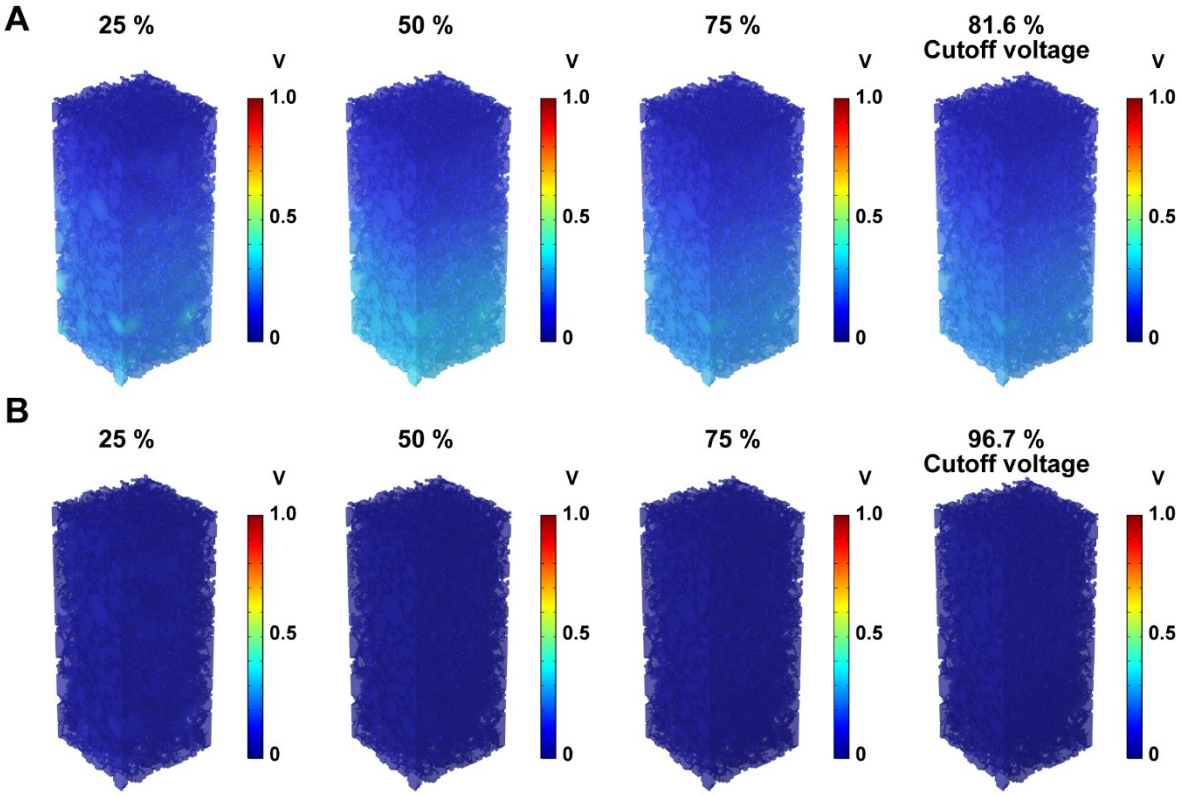

Fig. S14. 3D operando analysis of overpotentials in the active materials during charging at 2C under the realistic electrode condition and excessive electrolyte condition.
(A) 3D operando analysis of overpotential in active materials charged by 2C under the realistic electrode condition.
(B) 3D operando analysis of overpotential in active materials charged by 2C under the excessive electrolyte condition.

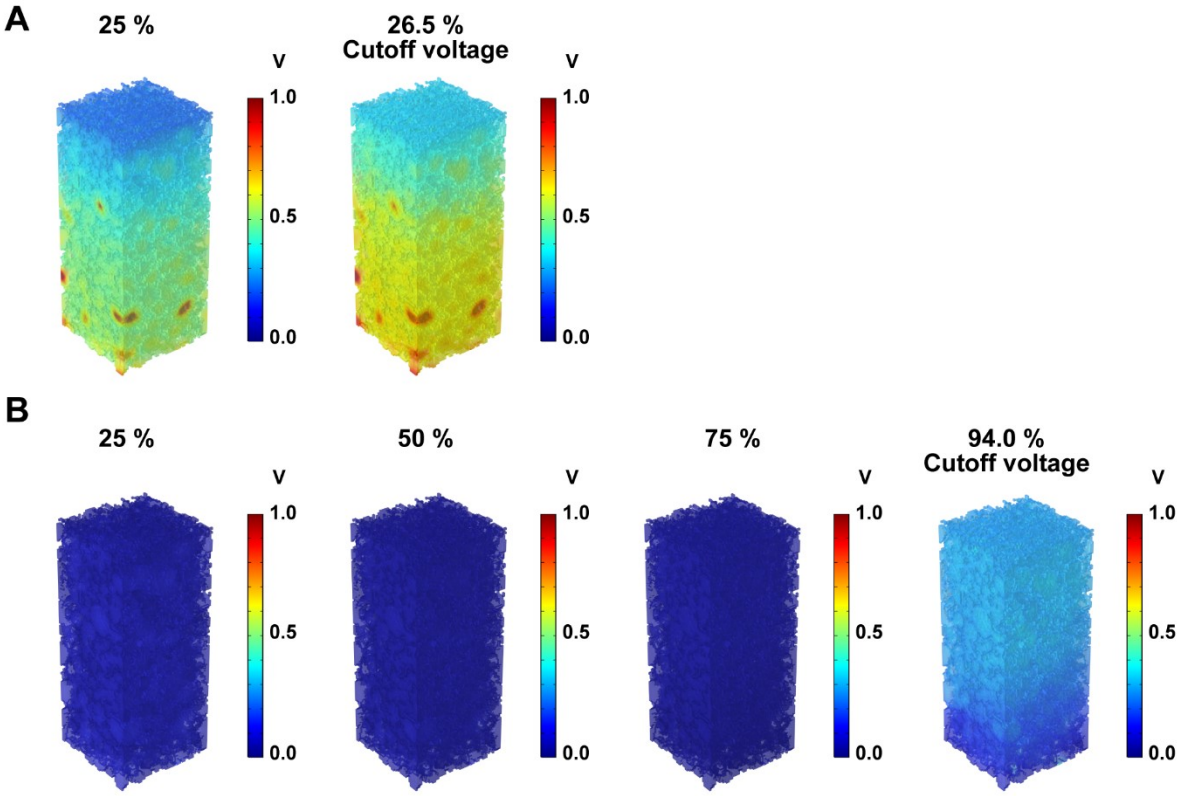

Fig. S15. 3D operando analysis of overpotentials in the active materials during charging at 4C under the realistic electrode condition and excessive electrolyte condition.
(A) 3D operando analysis of overpotential in active materials charged by 4C under the realistic electrode condition.
(B) 3D operando analysis of overpotential in active materials charged by 4C under the excessive electrolyte condition.

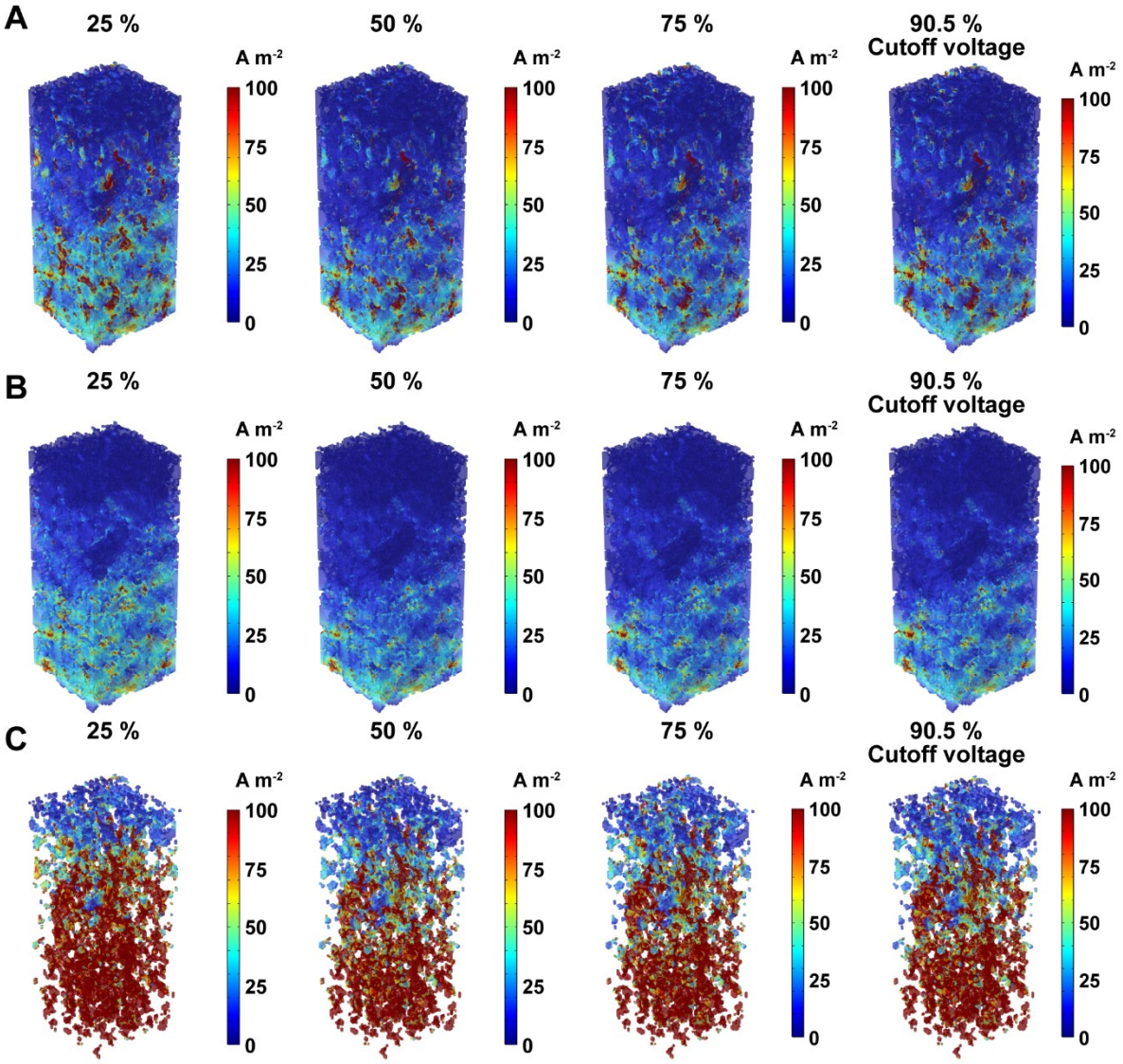

Fig. S16. 3D operando analysis of current densities during charging at 1C under the realistic electrode condition.
(A) 3D operando analysis of current densities in the total domains charged by 1C under the realistic electrode condition.
(B) 3D operando analysis of current densities in the active materials charged by 1C under the realistic electrode condition.
(C) 3D operando analysis of current densities in the conductive and binder materials charged by 1C under the realistic electrode condition.

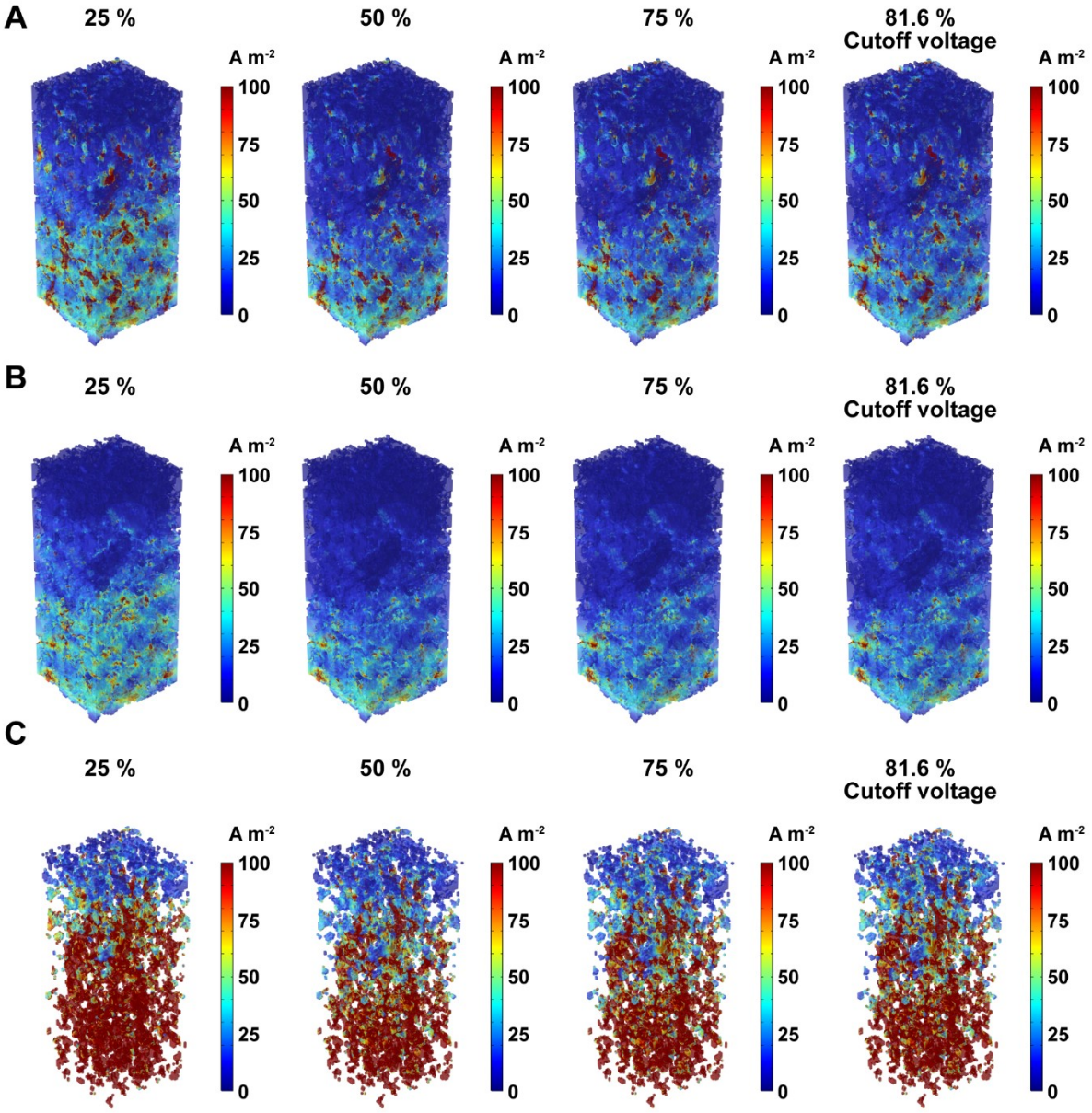

Fig. S17. 3D operando analysis of current densities during charging at 2C under the realistic electrode condition.

(A) 3D operando analysis of current densities in the total domains charged by 2C under the realistic electrode condition.

(B) 3D operando analysis of current densities in the active materials charged by 2C under the realistic electrode condition.

(C) 3D operando analysis of current densities in the conductive and binder materials charged by 2C under the realistic electrode condition.

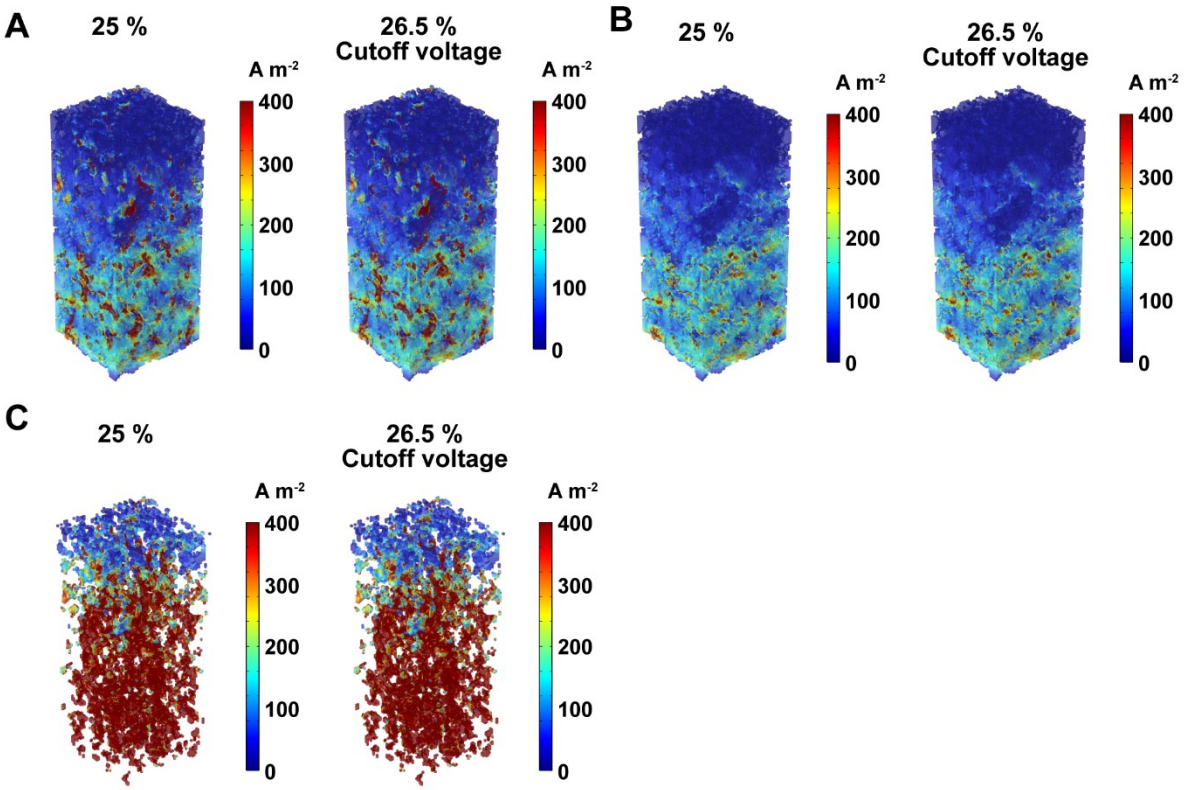

Fig. S18. 3D operando analysis of current densities during charging at 4C under the realistic electrode condition.

(A) 3D operando analysis of current densities in the total domains charged by 4C under the realistic electrode condition.

(B) 3D operando analysis of current densities in the active materials charged by 4C under the realistic electrode condition.

(C) 3D operando analysis of current densities in the conductive and binder materials charged by 4C under the realistic electrode condition.

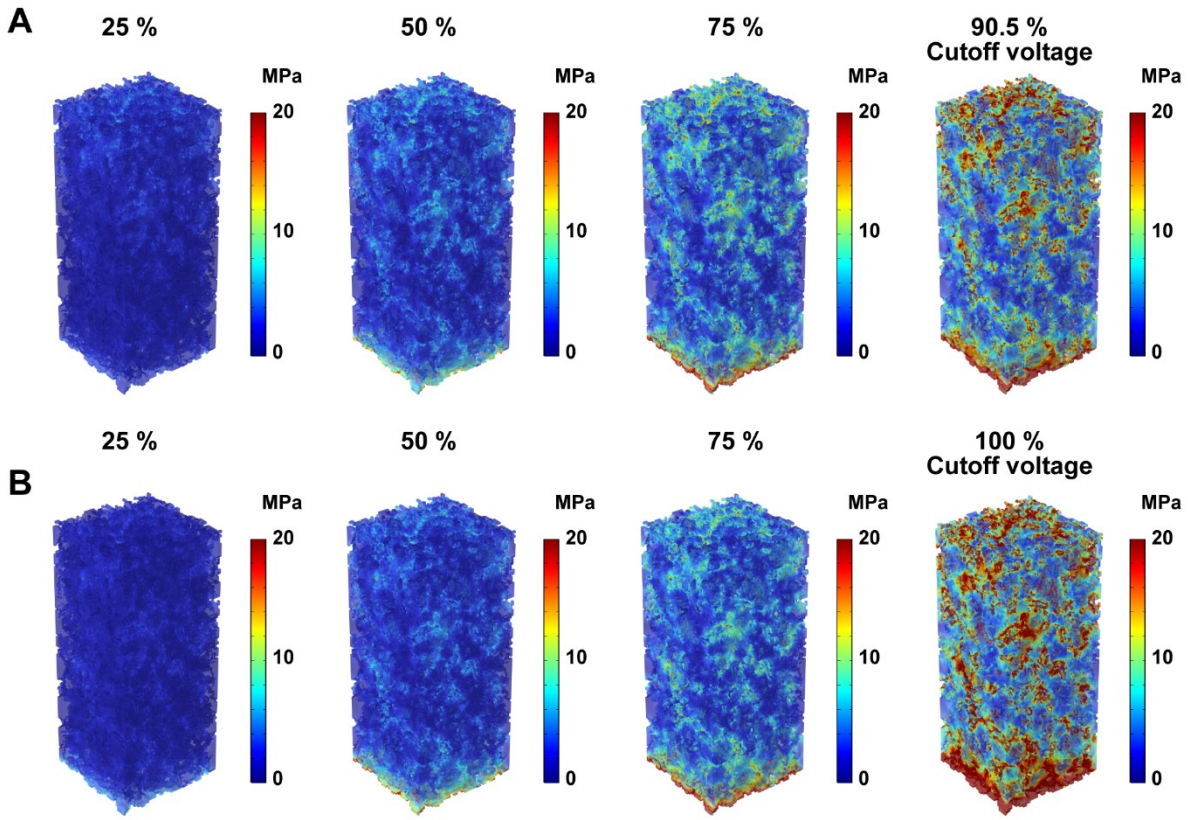

Fig. S19. 3D operando analysis of stress in active materials during charging at 1C under the realistic electrode condition and excessive electrolyte condition
(A) 3D operando analysis of von Mises stress in the active materials charged by 1C under the realistic electrode condition.
(B) 3D operando analysis of von Mises stress in the active materials charged by 1C under the excessive electrolyte condition.

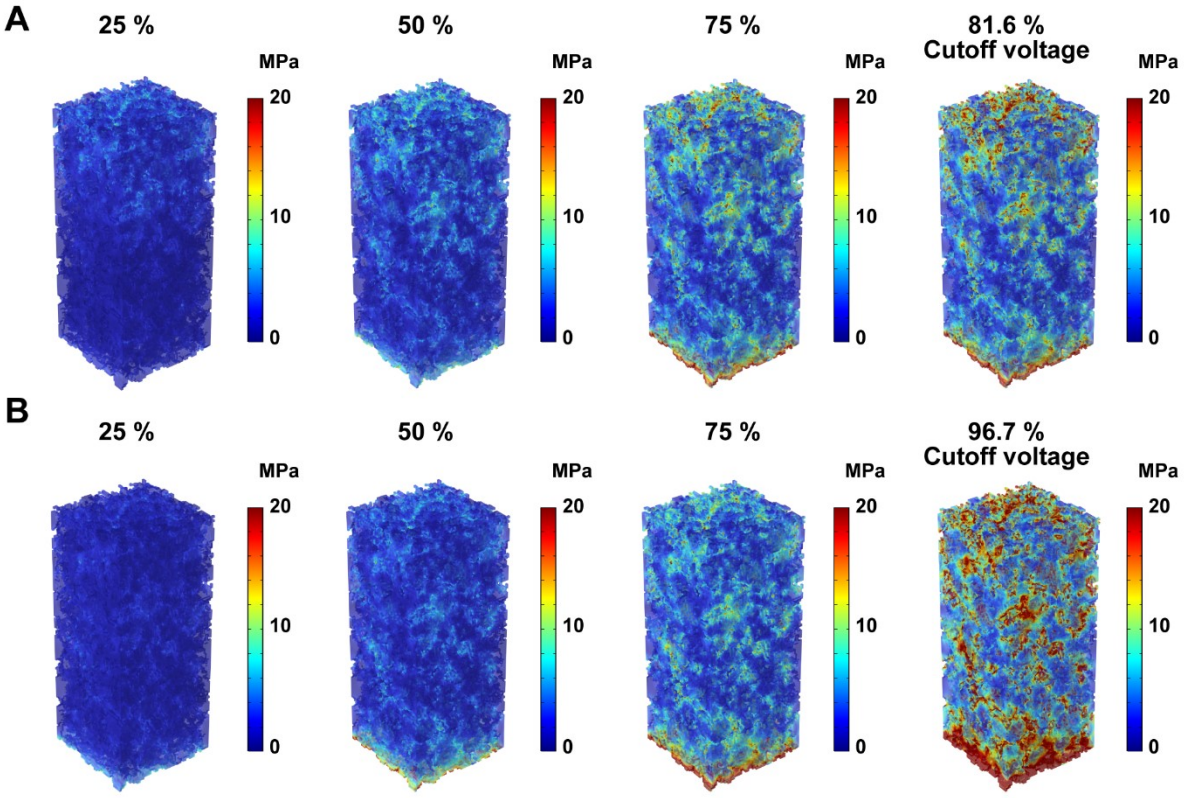

Fig. S20. 3D operando analysis of stress in active materials during charging at 2C under the realistic electrode condition and excessive electrolyte condition

(A) 3D operando analysis of von Mises stress in the active materials charged by 2C under the realistic electrode condition.

(B) 3D operando analysis of von Mises stress in the active materials charged by 2C under the excessive electrolyte condition.

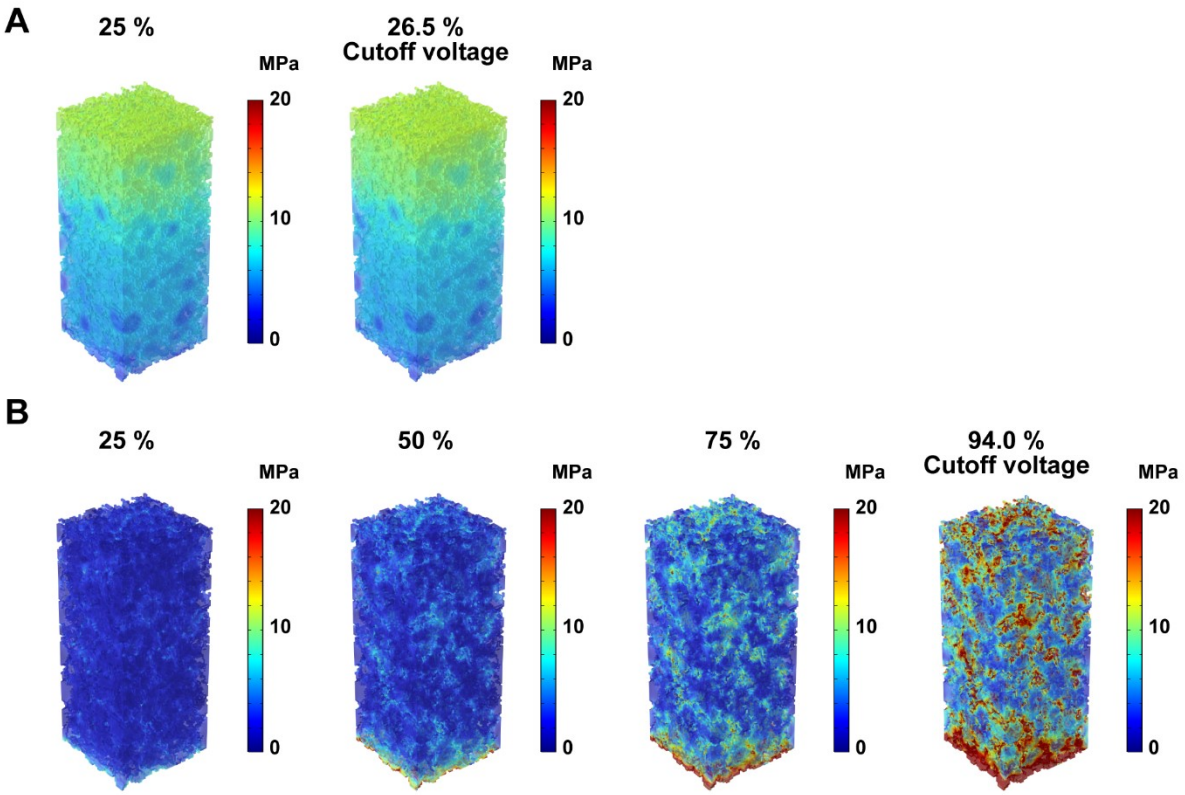

Fig. S21. 3D operando analysis of stress in active materials during charging at 4C under the realistic electrode condition and excessive electrolyte condition

(A) 3D operando analysis of von Mises stress in the active materials charged by 4C under the realistic electrode condition.

(B) 3D operando analysis of von Mises stress in the active materials charged by 4C under the excessive electrolyte condition.

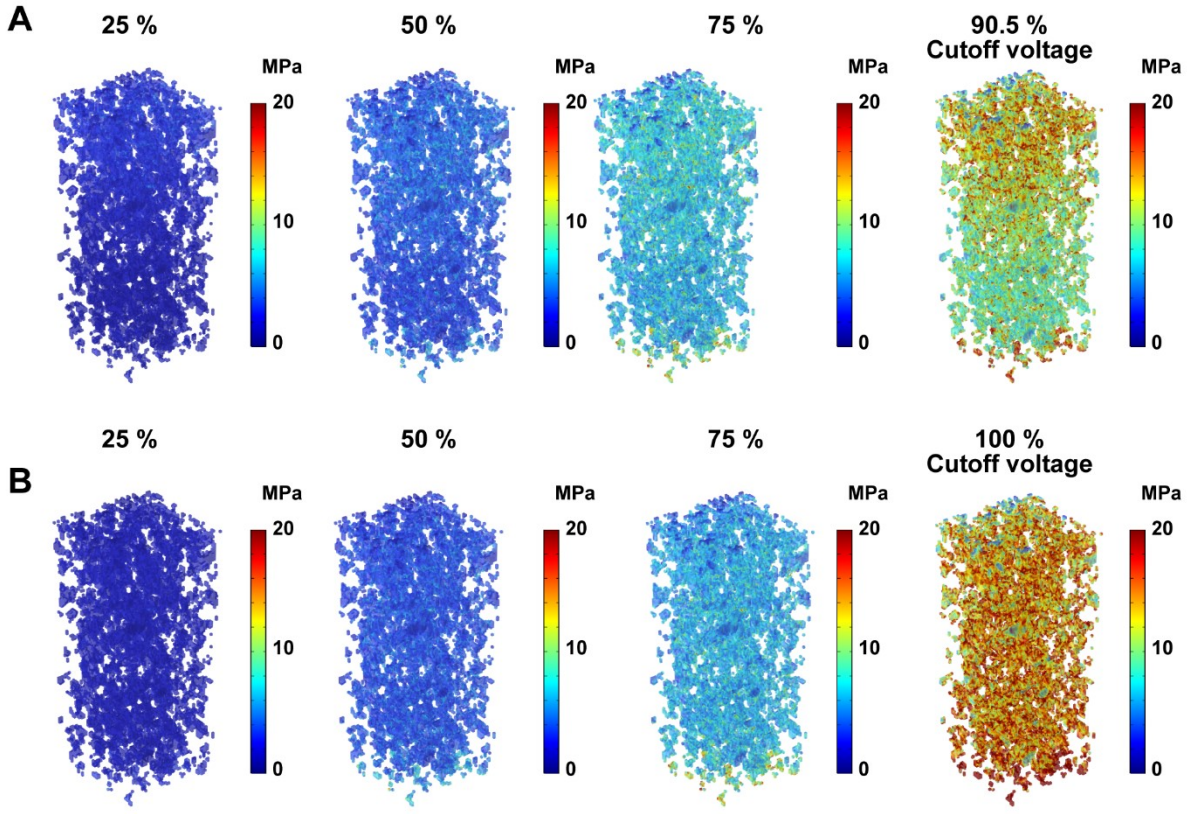

Fig. S22. 3D operando analysis of stress in conductive and binder materials during charging at 1C under the realistic electrode condition and excessive electrolyte condition
(A) 3D operando analysis of von Mises stress in the conductive and binder materials charged by 1C under the realistic electrode condition.
(B) 3D operando analysis of von Mises stress in the conductive and binder materials charged by 1C under the excessive electrolyte condition.

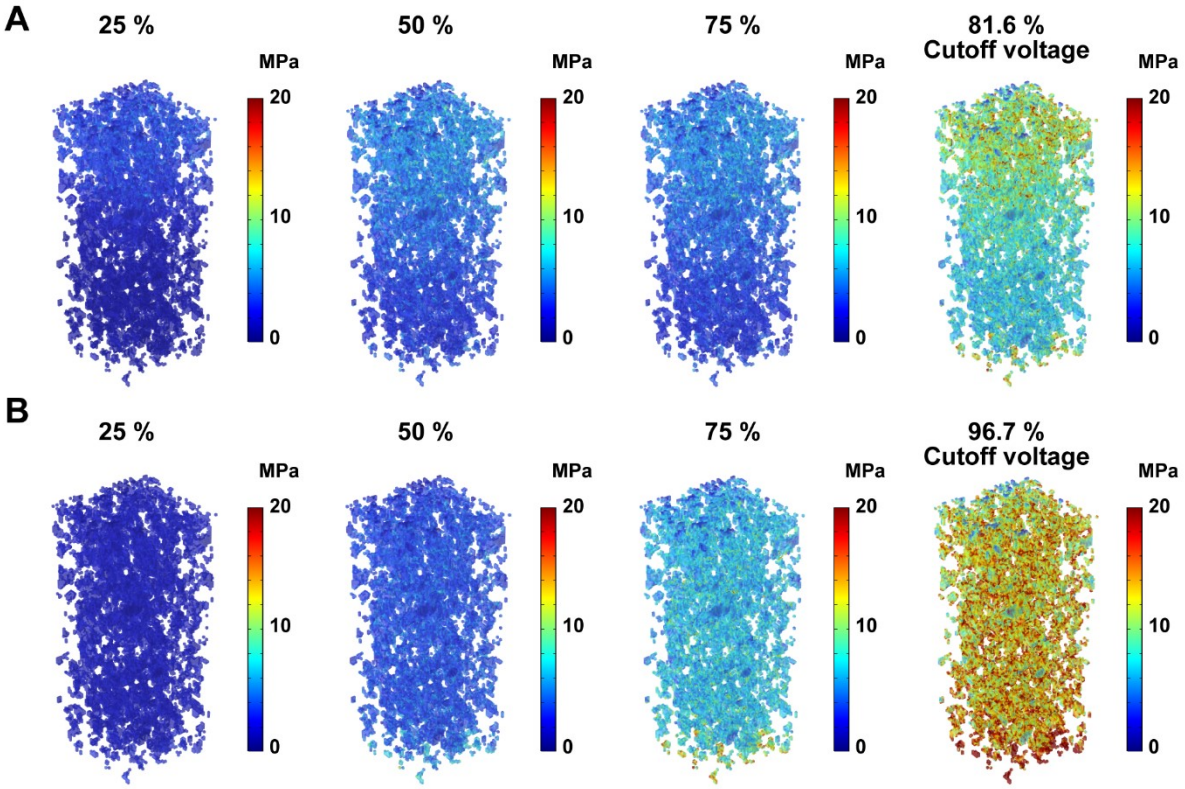

Fig. S23. 3D operando analysis of stress in conductive and binder materials during charging at 2C under the realistic electrode condition and excessive electrolyte condition
(A) 3D operando analysis of von Mises stress in the conductive and binder materials charged by 2C under the realistic electrode condition.
(B) 3D operando analysis of von Mises stress in the conductive and binder materials charged by 2C under the excessive electrolyte condition.

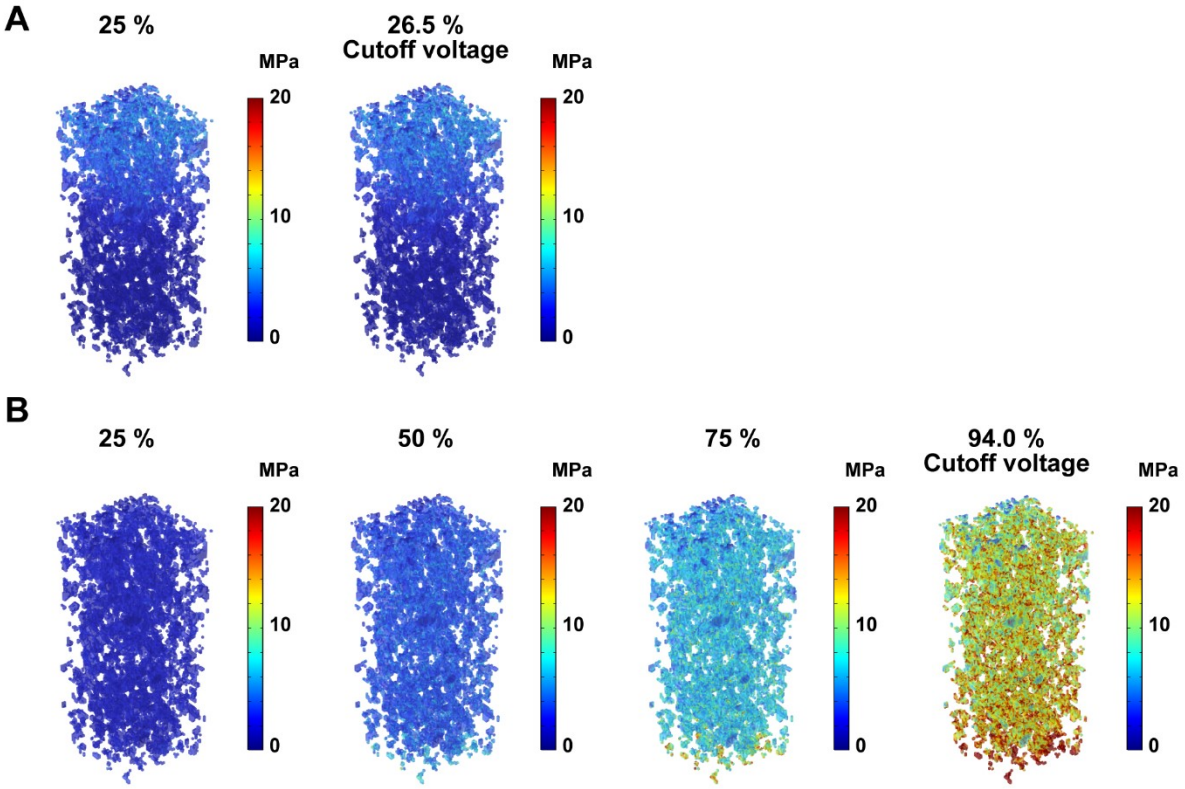

Fig. S24. 3D operando analysis of stress in conductive and binder materials during charging at 4C under the realistic electrode condition and excessive electrolyte condition
(A) 3D operando analysis of von Mises stress in the conductive and binder materials charged by 4C under the realistic electrode condition.
(B) 3D operando analysis of von Mises stress in the conductive and binder materials charged by 4C under the excessive electrolyte condition.

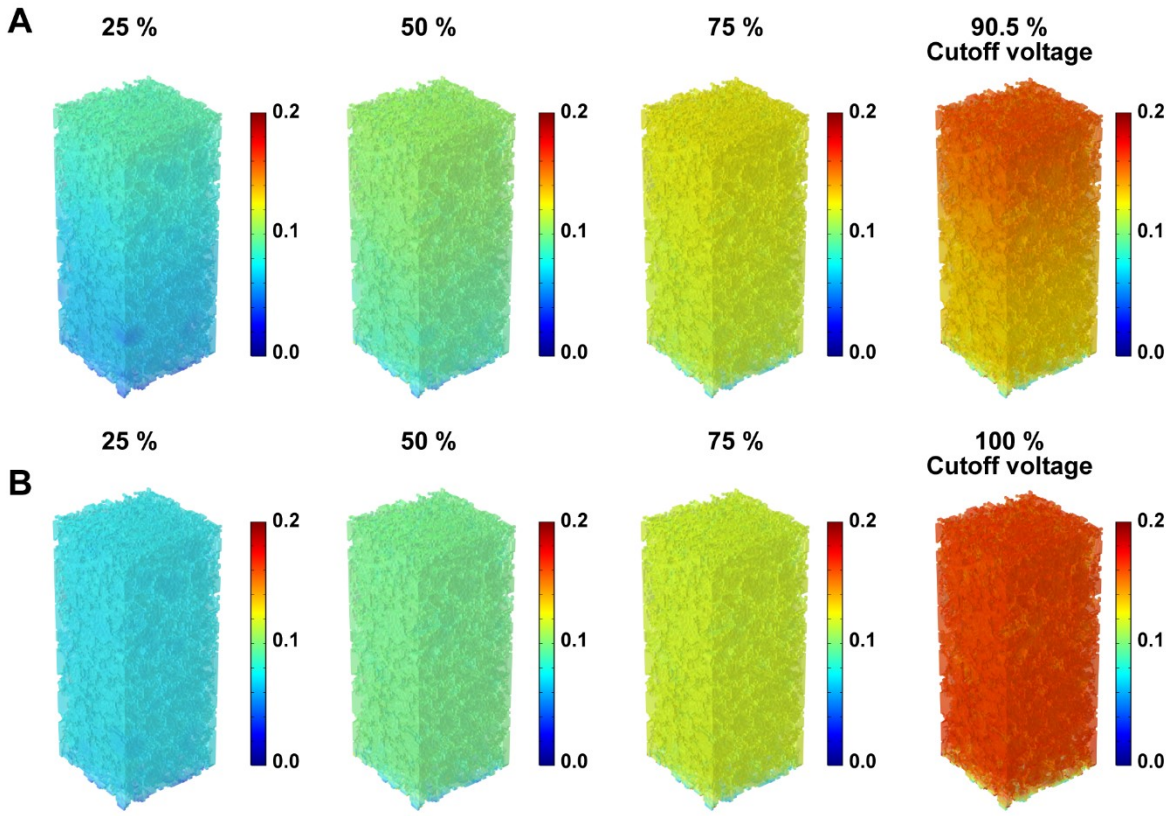

Fig. S25. 3D operando analysis of strain in active materials during charging at 1C under the realistic electrode condition and excessive electrolyte condition

(A) 3D operando analysis of strain in the active materials charged by 1C under the realistic electrode condition.

(B) 3D operando analysis of strain in the active materials charged by 1C under the excessive electrolyte condition.

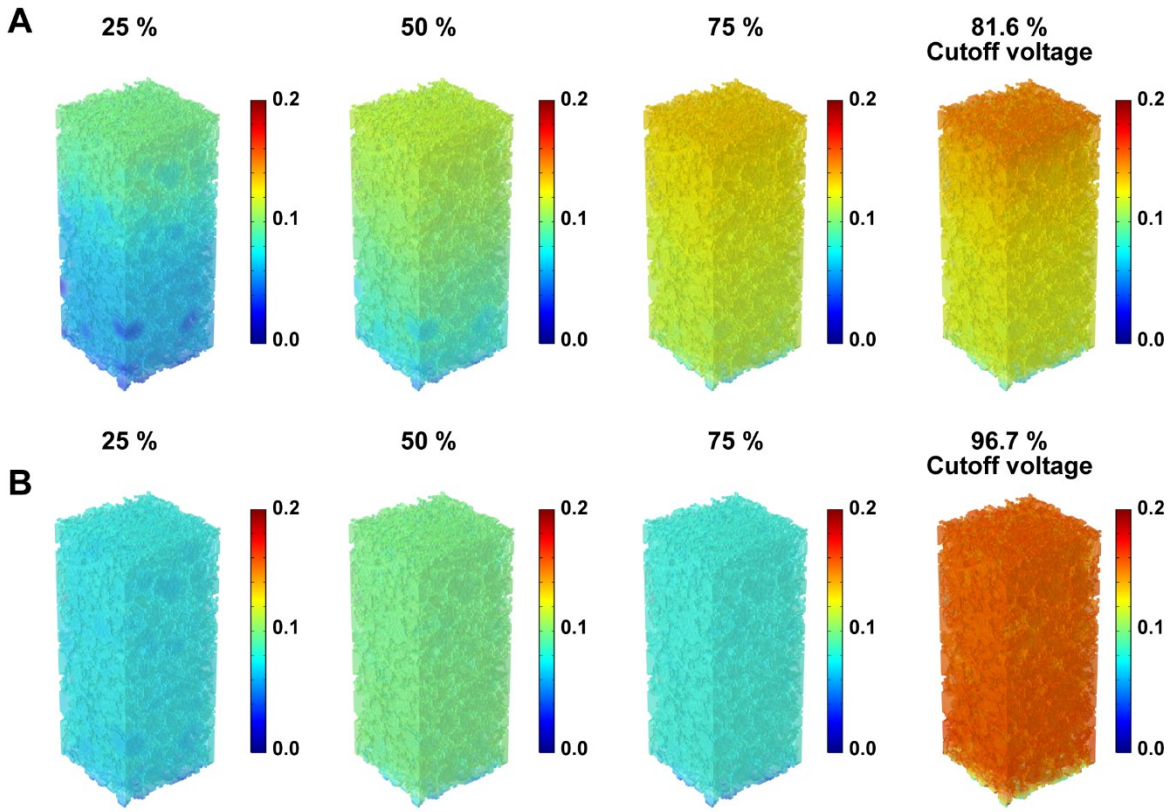

Fig. S26. 3D operando analysis of strain in active materials during charging at 2C under the realistic electrode condition and excessive electrolyte condition

(A) 3D operando analysis of strain in the active materials charged by 2C under the realistic electrode condition.

(B) 3D operando analysis of strain in the active materials charged by 2C under the excessive electrolyte condition.

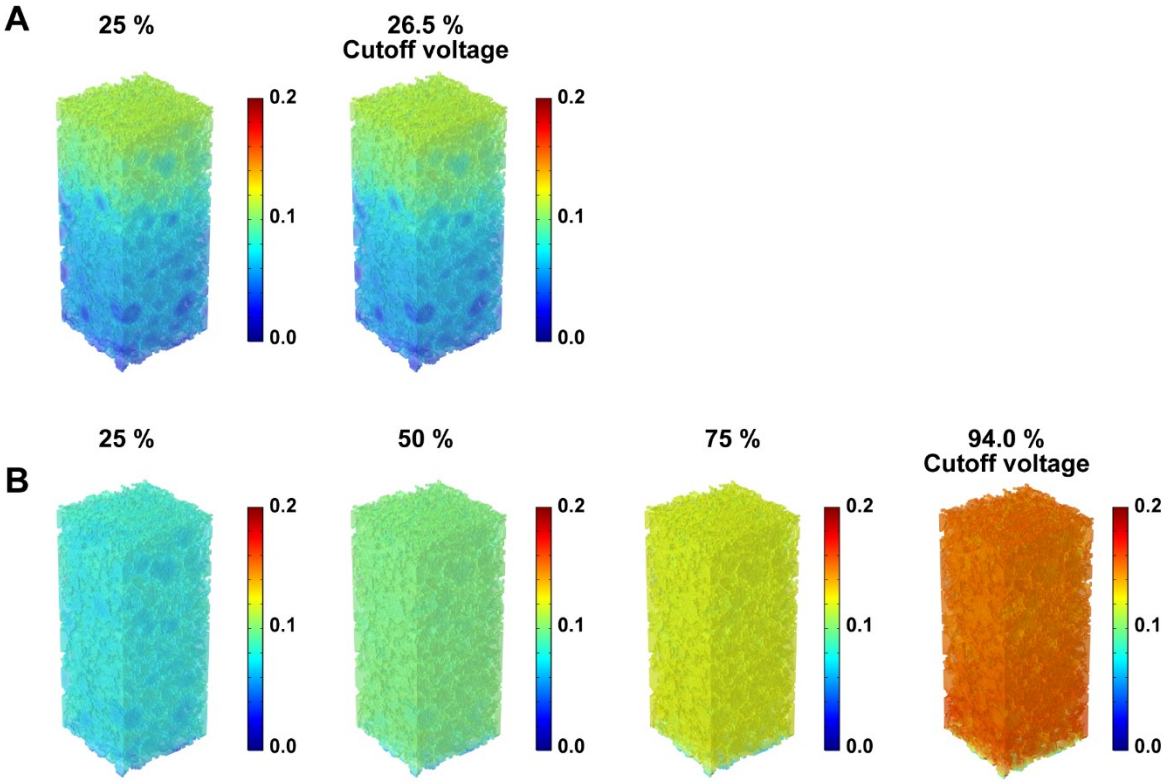

Fig. S27. 3D operando analysis of strain in active materials during charging at 4C under the realistic electrode condition and excessive electrolyte condition

(A) 3D operando analysis of strain in the active materials charged by 4C under the realistic electrode condition.

(B) 3D operando analysis of strain in the active materials charged by 4C under the excessive electrolyte condition.

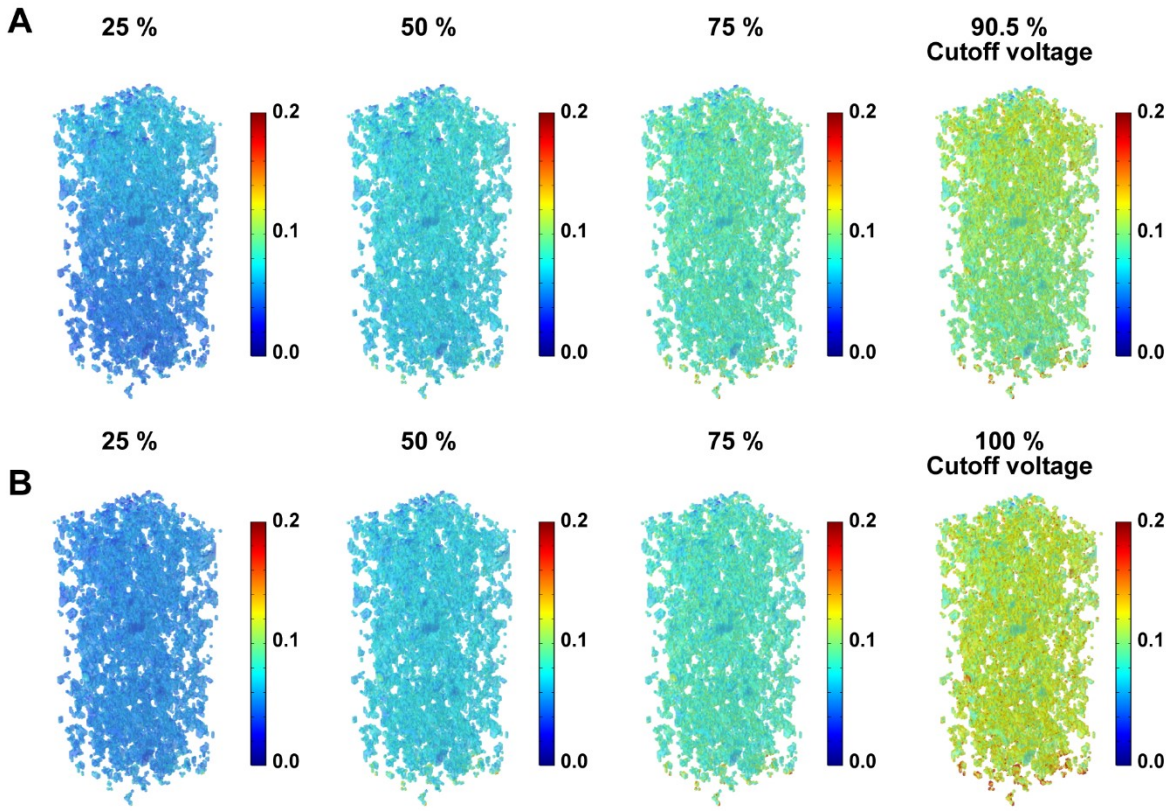

Fig. S28. 3D operando analysis of strain in conductive and binder materials during charging at 1C under the realistic electrode condition and excessive electrolyte condition
(A) 3D operando analysis of strain in the conductive and binder materials charged by 1C under the realistic electrode condition.
(B) 3D operando analysis of strain in the conductive and binder materials charged by 1C under the excessive electrolyte condition.

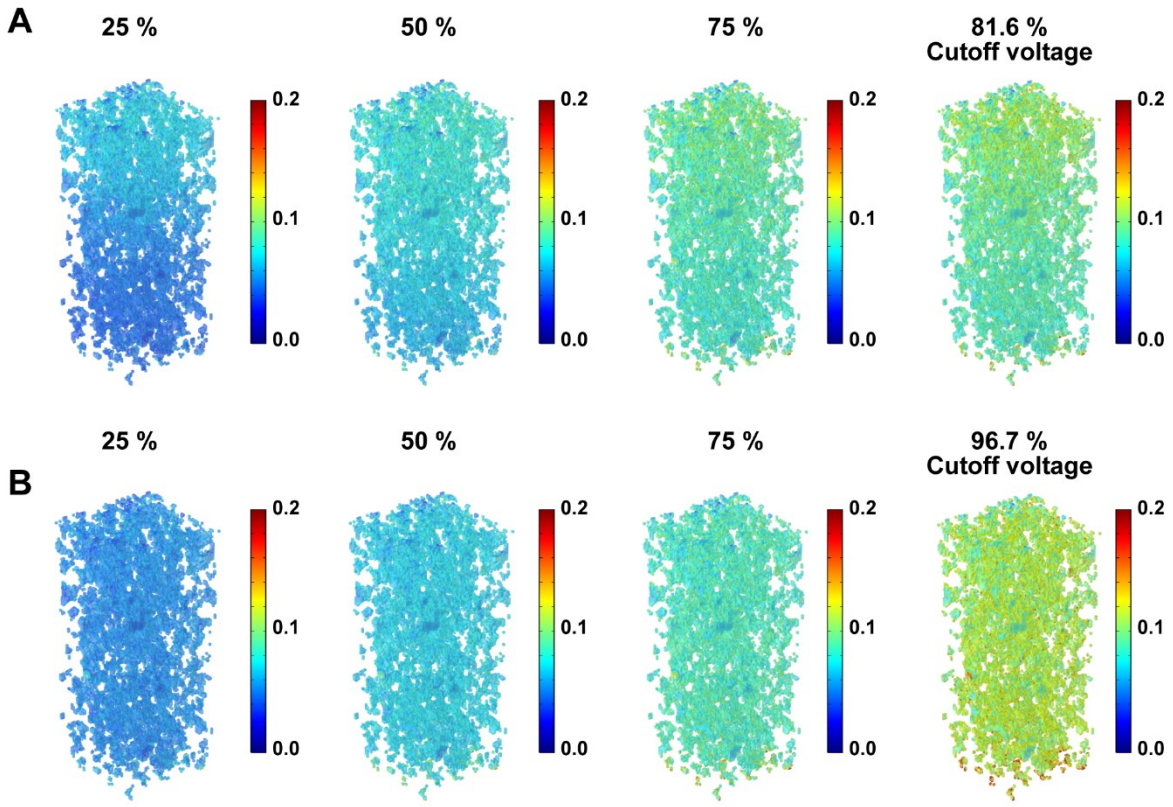

Fig. S29. 3D operando analysis of strain in conductive and binder materials during charging at 2C under the realistic electrode condition and excessive electrolyte condition
(A) 3D operando analysis of strain in the conductive and binder materials charged by 2C under the realistic electrode condition.
(B) 3D operando analysis of strain in the conductive and binder materials charged by 2C under the excessive electrolyte condition.

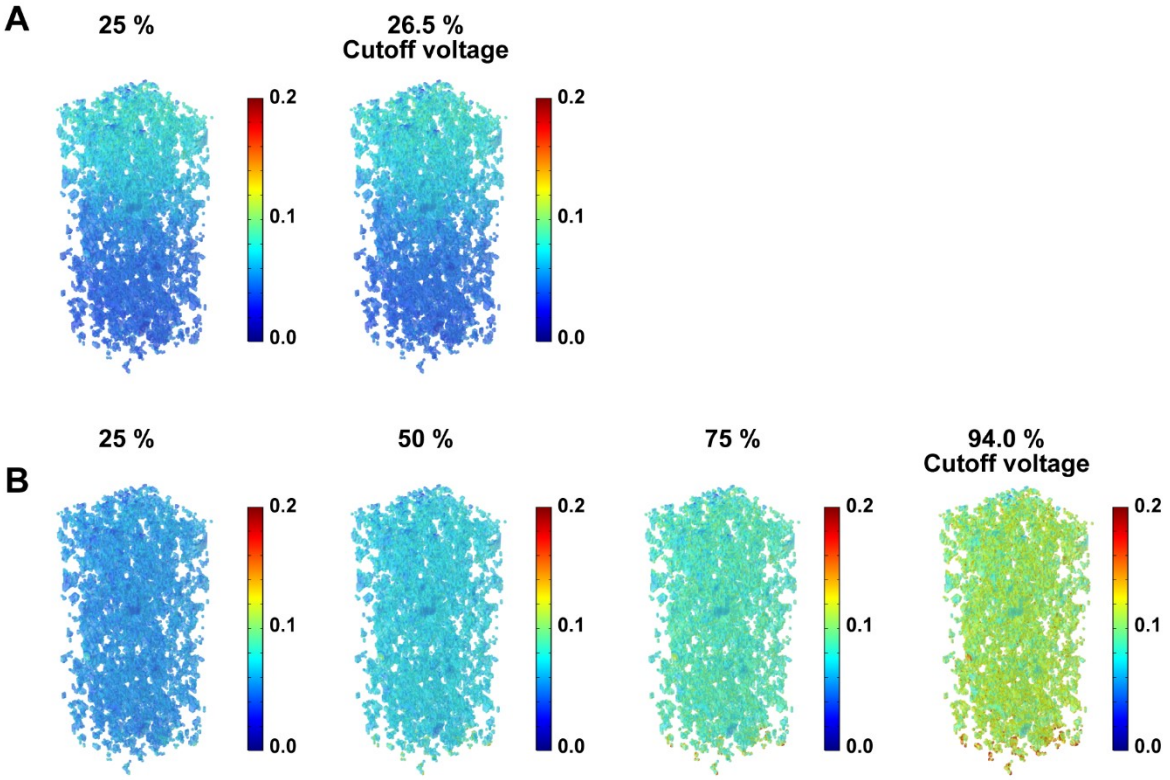

Fig. S30. 3D operando analysis of strain in conductive and binder materials during charging at 4C under the realistic electrode condition and excessive electrolyte condition
(A) 3D operando analysis of strain in the conductive and binder materials charged by 4C under the realistic electrode condition.
(B) 3D operando analysis of strain in the conductive and binder materials charged by 4C under the excessive electrolyte condition.

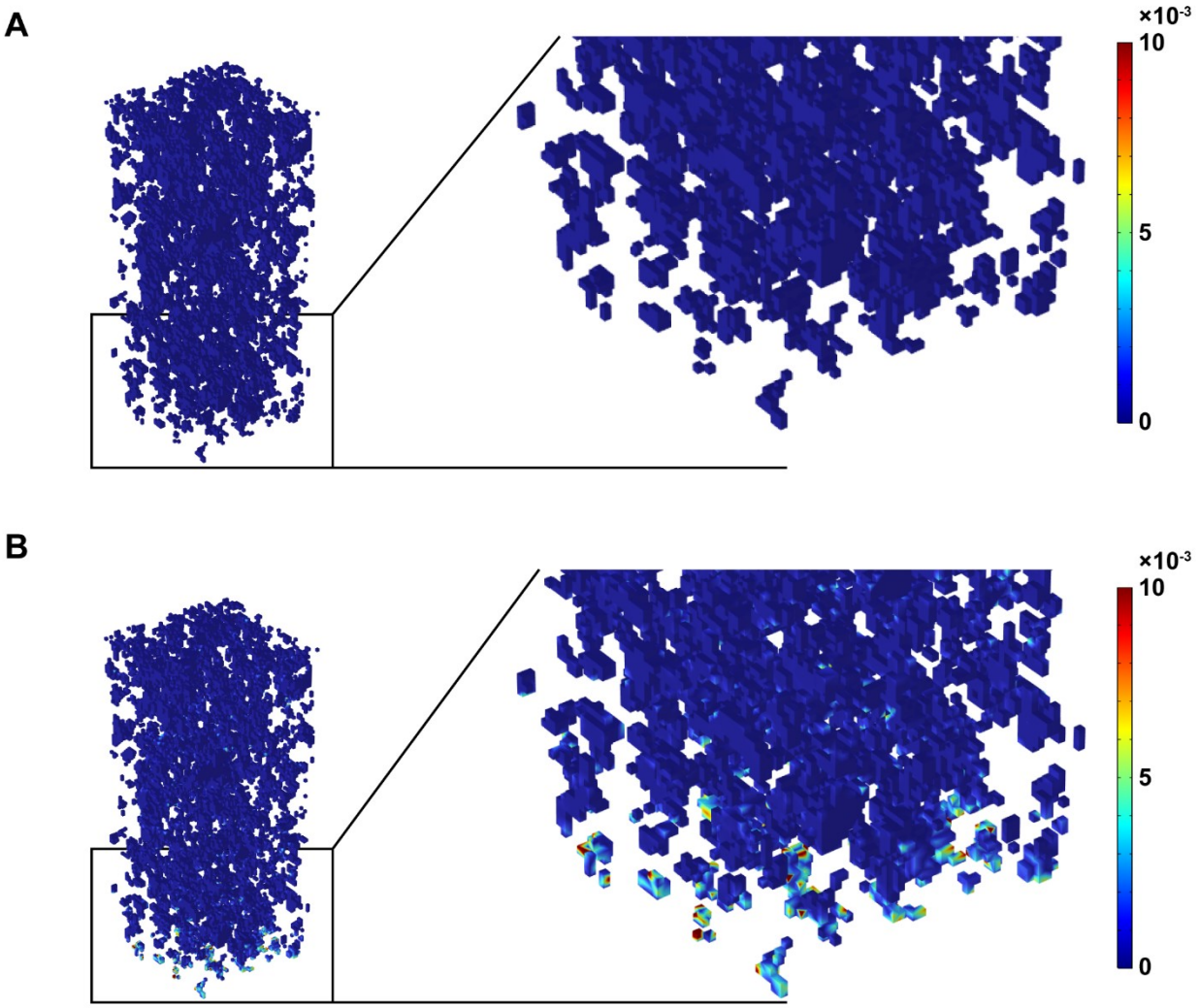

Fig. S31. 3D operando analysis of plastic deformations at the end of charge at 4C under the realistic electrode condition and excessive electrolyte condition.
(A) 3D operando analysis of plastic deformation at the end of charge at 4C under the realistic electrode condition.
(B) 3D operando analysis of plastic deformation at the end of charge at 4C under the excessive electrolyte condition.

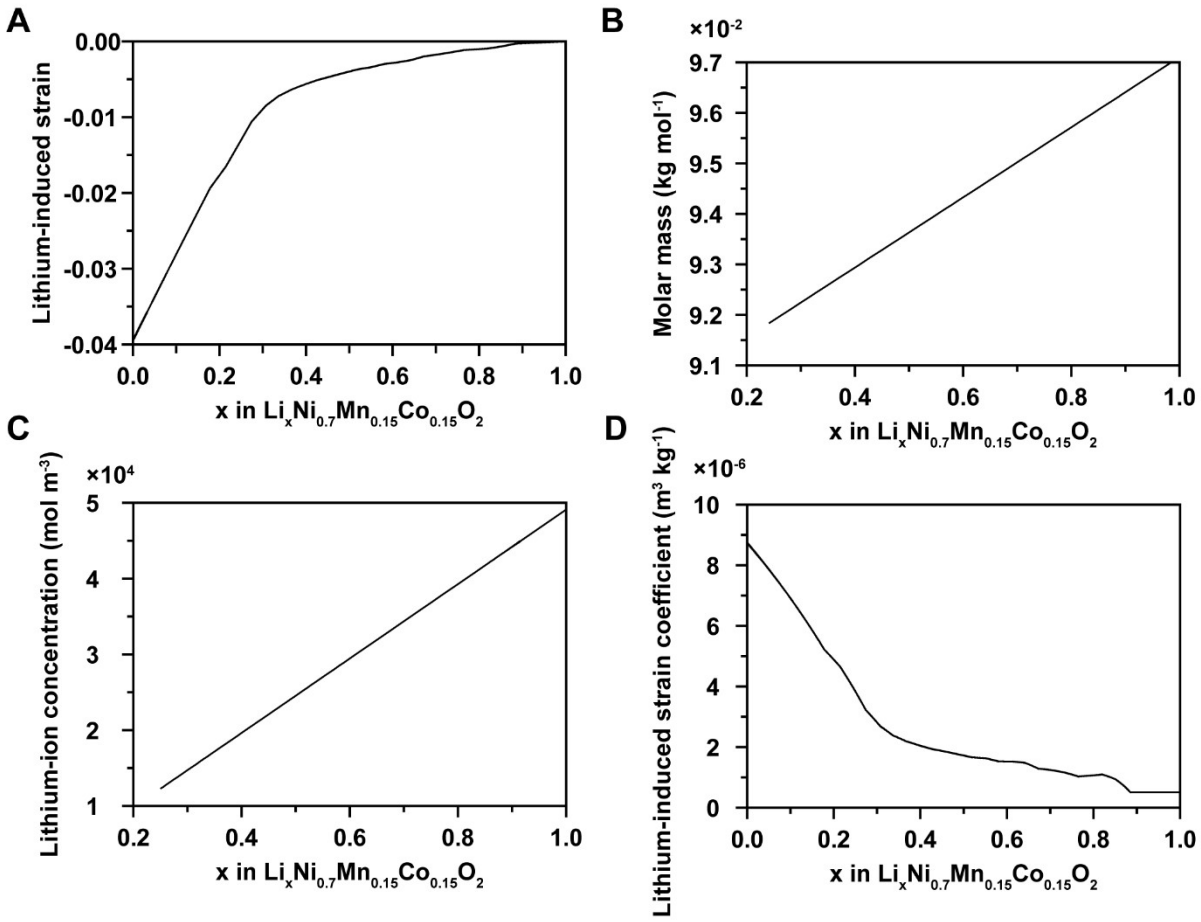

Fig. S32. Hygroscopic swelling parameters.
(A) The lithium-induced strain calculated from volume change.
(B) Molar mass.
(C) Lithium-ion concentration.
(D) Lithium-induced strain coefficient derived inversely by applying lithium-induced strain, molar mass, and lithium-ion concentration changes to the hygroscopic swelling equation.

Video S1. 2D operando analysis of lithium-ion concentration of (A) active materials and (B) electrolyte, (C) overpotential, and (D) current density at 1C in the middle of the composite electrode under the excessive electrolyte condition.
Video S2. 2D operando analysis of lithium-ion concentration of (A) active materials and (B) electrolyte, (C) overpotential, and (D) current density at 1C in the middle of the composite electrode under the realistic electrode condition.
Video S3. 3D operando von Mises stress at 4C under the realistic electrode condition.
Video S4. 3D operando von Mises stress at 4C under the excessive electrolyte condition